Biophysical Journal
Article

Biophysical Society

Regulation of K-Ras4B Membrane Binding by Calmodulin

Benjamin Sperlich,[1] Shobhna Kapoor,[2,3] Herbert Waldmann,[2,3] Roland Winter,[1,*] and Katrin Weise[1,*]
[1]Physical Chemistry I – Biophysical Chemistry and [2]Chemical Biology, TU Dortmund University, Dortmund, Germany; and [3]Department of Chemical Biology, Max Planck Institute of Molecular Physiology, Dortmund, Germany

ABSTRACT K-Ras4B is a membrane-bound small GTPase with a prominent role in cancer development. It contains a polybasic farnesylated C-terminus that is required for the correct localization and clustering of K-Ras4B in distinct membrane domains. PDEδ and the Ca^{2+}-binding protein calmodulin (CaM) are known to function as potential binding partners for farnesylated Ras proteins. However, they differ in the number of interaction sites with K-Ras4B, leading to different modes of interaction, and thus affect the subcellular distribution of K-Ras4B in different ways. Although it is clear that Ca^{2+}-bound CaM can play a role in the dynamic spatial cycle of K-Ras4B in the cell, the exact molecular mechanism is only partially understood. In this biophysical study, we investigated the effect of Ca^{2+}/CaM on the interaction of GDP- and GTP-loaded K-Ras4B with heterogeneous model biomembranes by using a combination of different spectroscopic and imaging techniques. The results show that Ca^{2+}/CaM is able to extract K-Ras4B from negatively charged membranes in a nucleotide-independent manner. Moreover, the data demonstrate that the complex of Ca^{2+}/CaM and K-Ras4B is stable in the presence of anionic membranes and shows no membrane binding. Finally, the influence of Ca^{2+}/CaM on the interaction of K-Ras4B with membranes is compared with that of PDEδ, which was investigated in a previous study. Although both CaM and PDEδ exhibit a hydrophobic binding pocket for farnesyl, they have different effects on membrane binding of K-Ras4B and hence should be capable of regulating K-Ras4B plasma membrane localization in the cell.

INTRODUCTION

Ras GTPases are key regulators of signal transduction pathways that control cell proliferation, differentiation, survival, and apoptosis. As binary molecular switches, they cycle between inactive and active nucleotide-bound states at the plasma membrane, linking extracellular signals through membrane receptors to intracellular signaling cascades (1–4). Among the activating mutations in *Ras* genes, K-Ras mutations are predominant, with K-Ras4B mutations occurring in up to 90% of pancreatic tumors, 57% of colorectal tumors, and 50% of lung cancers (cf. Ref. (5) and references therein) (6,7). The 4B splice variant of K-Ras (K-Ras4B) is localized to the cytoplasmic, negatively charged leaflet of the plasma membrane by a farnesylated and polybasic targeting sequence within its hypervariable region (2,8–11) (Fig. 1 *A*). Recent results revealed an essential role of the cytosolic, GDI-like solubilizing factor GMP phosphodiesterase 6 delta subunit (PDEδ) in the plasma membrane localization of K-Ras4B, whereby the Arl2-PDEδ perinuclear membrane delivery system seems to regulate a dynamic spatial cycle of K-Ras4B in the cell (12–14). The hydrophobic pocket of PDEδ binds and solubilizes farnesylated K-Ras4B proteins irrespective of the bound nucleotide state, thereby facilitating their cytoplasmic diffusion (12,14). Moreover, it was suggested that K-Ras4B can be redirected from the plasma membrane to intracellular membranes through a Ca^{2+}-calmodulin (CaM)-dependent pathway (15). Ca^{2+}-loaded CaM (Ca^{2+}/CaM) specifically binds the Ras isoform K-Ras4B and modulates its downstream signaling (15–17).

The calcium-modulated protein CaM is a small, highly conserved, intracellular, acidic EF-hand protein that is present in many eukaryotic cells (18–20). Binding of Ca^{2+}/CaM to its target proteins is enabled mainly by hydrophobic interactions of hydrophobic patches that become exposed in its Ca^{2+}-loaded state (21). Electrostatic interactions contribute to the stability of the Ca^{2+}/CaM target complex and have been suggested to play an important role in target recognition (18,22,23). However, the crystal structure of Ca^{2+}/CaM bound to a myristoylated peptide revealed a different binding mode. Whereas the conformation of Ca^{2+}/CaM is similar to those of other Ca^{2+}/CaM-peptide

Submitted February 1, 2016, and accepted for publication May 24, 2016.
*Correspondence: roland.winter@tu-dortmund.de or katrin.weise@tu-dortmund.de
Editor: Heiko Heerklotz
http://dx.doi.org/10.1016/j.bpj.2016.05.042

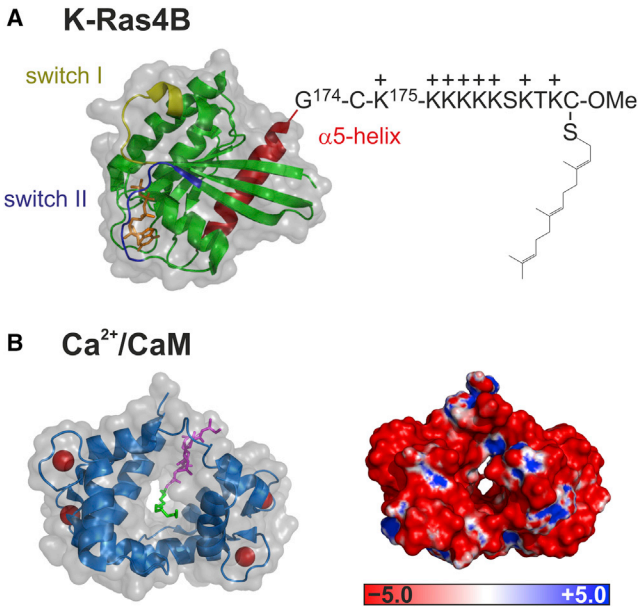

FIGURE 1 Schematic representation of the semisynthetic K-Ras4B protein and Ca^{2+}/CaM (PDB: 3GFT and 1L7Z, respectively). (*A*) The synthesized, lipidated K-Ras4B peptide was ligated to a truncated K-Ras4B protein expressed in *Escherichia coli* to yield the *S*-farnesylated K-Ras4B protein bearing an additional cysteine between Gly174 and Lys175 (30). (*B*) The left image shows the crystal structure of Ca^{2+}/CaM in complex with a myristoylated peptide. The N- and C-terminal domains of CaM are shown in blue and the four bound Ca^{2+} ions are shown as red spheres. The myristoyl group (*green*) goes through the hydrophobic tunnel of Ca^{2+}/CaM, and the peptide consisting of GGKLSK (*purple*) is located along the groove between the two lobes of Ca^{2+}/CaM (24). On the right, an Adaptive Poisson-Boltzmann Solver-generated electrostatic surface of Ca^{2+}/CaM is displayed with the use of PyMOL (58). The positive (*blue*) and negative (*red*) electrostatic potential isocontours were set to +5 and −5 $k_BT\,e^{-1}$, respectively.

complexes, the N-terminal myristoyl group was found to be firmly anchored to Ca^{2+}/CaM by multiple hydrophobic interactions, i.e., it is accommodated in a large hydrophobic cavity created by the hydrophobic pockets of the N- and C-terminal domains of Ca^{2+}/CaM (Fig. 1 *B*, *left*). In addition, intermolecular electrostatic interactions were shown to play a significant role. When the peptide is located along the groove between the two lobes of CaM, the C-terminal basic cluster of the peptide (myr-GGKLSKKKK) becomes surrounded by many acidic residues of CaM (24).

There is evidence that Ca^{2+}/CaM binds to K-Ras4B and dissociates it from membranes independently of the nucleotide state of K-Ras4B (15,25). In contrast, a recent study observed that inhibition of Ca^{2+}/CaM reduced the rate of dissociation from the plasma membrane for active K-Ras4B only (26). In solution, an equimolar, GTP-dependent binding of K-Ras4B to Ca^{2+}/CaM, with micromolar affinity, was detected (16,17,27). Previous studies revealed that at least three different regions of K-Ras4B are important for the interaction with Ca^{2+}/CaM: 1) the hypervariable region as the primary binding site, with both the farnesyl group and polybasic sequence being essential for binding; 2) the amphipathic helix α5; and 3) the switch II region (which could explain the observed GTP dependence) (15,17,27,28). Although the importance of farnesylation for binding of K-Ras4B to CaM is well established (15,28), no crystal structure of such a complex is available so far. However, in a study by Matsubara et al. (24), the crystal structure of Ca^{2+}/CaM in complex with a myristoylated peptide that also contains a polybasic stretch of lysines (myr-GGKLSKKKK) revealed an ellipsoidal, compact structure for CaM, whose hydrophobic cavity is mainly filled with the myristoyl moiety (cf. Fig. 1 *B*). These authors also demonstrated that CaM residues within 5 Å of the myristoyl group are mainly hydrophobic, and that multiple hydrophobic interactions are responsible for binding. The binding interface of the myristoyl group in the hydrophobic tunnel of the CaM complex is shown in Fig. S1 in the Supporting Material. The space model indicates that although the farnesyl residue is unsaturated and branched (in contrast to myristoyl), the myristoyl-binding pocket is large enough to also accommodate the bulkier farnesyl moiety.

Although it is clear that Ca^{2+}/CaM can regulate K-Ras4B cycling, the exact molecular mechanism is only partially understood. In this study, we sought to determine whether Ca^{2+}/CaM directly extracts K-Ras4B from membranes or binds K-Ras4B only after its dissociation from heterogeneous model membranes. In particular, we investigated the debated nucleotide dependence of the process. A combination of different biophysical techniques, namely, surface plasmon resonance (SPR), atomic force microscopy (AFM), infrared reflection absorption spectroscopy (IRRAS), and fluorescence anisotropy, was used. An analysis of the interaction of K-Ras4B with Ca^{2+}/CaM in the absence and presence of heterogeneous model membranes revealed that Ca^{2+}/CaM can extract membrane-bound K-Ras4B independently of its nucleotide-bound state, contrary to what was observed in a previous study of PDEδ (29).

MATERIALS AND METHODS

Materials and sample preparation

The phospholipids 1,2-dioleoyl-*sn*-glycero-3-phosphocholine (DOPC), 1,2-dioleoyl-*sn*-glycero-3-phospho-(1′-*rac*-glycerol) sodium salt (DOPG), 1,2-dipalmitoyl-*sn*-glycero-3-phospho-(1′-*rac*-glycerol) sodium salt (DPPG), and 1,2-dipalmitoyl-*sn*-glycero-3-phosphocholine (DPPC) were purchased from Avanti Polar Lipids (Alabaster, AL) as lyophilized powders. Cholesterol (Chol) and 4-(2-hydroxyethyl)piperazine-1-ethanesulfonic acid (Hepes) were obtained from Sigma Aldrich (Deisenhofen, Germany). Magnesium chloride, tris(hydroxymethyl)-aminomethan (Tris), chloroform, and CaM (bovine brain) were obtained from Merck (Darmstadt, Germany); bovine serum albumin from Pierce (Bonn, Germany). The fluorescent marker 5-(dimethylamino)naphthalene-1-sulfonyl chloride (dansyl chloride) was purchased from Life Technologies (Darmstadt, Germany) and 1,4-bis(5-phenyloxazol-2-yl)benzene was obtained from Alfa Aesar (Karlsruhe, Germany). Details regarding the formation of large unilamellar vesicles (100 nm in size) can be found in Supporting Material.

Protein synthesis and purification

The synthesis of K-Ras4B proteins has been described in detail before (30). Briefly, the *S*-farnesylated K-Ras4B protein was synthesized by a combination of expressed protein ligation and lipopeptide synthesis. Nucleotide exchange (GppNHp-bound state as a nonhydrolyzable GTP analog) was carried out as described before (31). Dansyl labeling of CaM was performed by incubating 5 mg protein in 250 μL buffer (100 mM $NaHCO_3$, 1 mM $CaCl_2$, pH 8.5) with a fivefold molar excess of dansyl chloride for 2 h at 4°C. Unbound fluorophores were removed with the use of a 5 mL HiTrap desalting column (GE Healthcare, Freiburg, Germany). A degree of labeling of 46% was determined by absorbance measurements at 280 nm ($\varepsilon_{280} = 3345\ M^{-1}\ cm^{-1}$) and 340 nm ($\varepsilon_{340} = 3400\ M^{-1}\ cm^{-1}$).

SPR

SPR experiments were carried out with a Biacore 3000 system (Biacore, Uppsala, Sweden; now GE Healthcare). For the protein-membrane interaction studies, the L1 sensor chip (GE Healthcare) was used. Details on sample preparation, vesicle immobilization, performance of SPR measurements, regeneration of the chip surface, and analysis of the SPR sensorgrams have been described before (29,32) and are given in Supporting Materials and Methods. For the curve-fitting procedure, BIAevaluation software 4.1 (Biacore, Uppsala, Sweden) and Origin 8.6 (OriginLab, Northampton, MA) were used.

IRRAS

IRRAS experiments were carried out on a setup consisting of two linked Teflon troughs and a Vertex 70 Fourier transform infrared (FT-IR) spectrometer connected to an A511 reflection attachment (both Bruker, Germany) with an MCT detector. The measurements were performed according to the setup, sample preparation, and spectra analysis described before (29,31). The temperature of the subphase was maintained at 20°C ± 0.5°C and time-dependent measurements were performed in the small (reference) trough at a constant surface area. The resulting curve of surface pressure versus time is referred to as the π/t isotherm. Both troughs were filled with 20 mM Tris, 7 mM $MgCl_2$, 1 mM $CaCl_2$, pD 7.4. Monolayers of DOPC/DOPG/DPPC/DPPG/Chol 20:5:45:5:25 (mol%) were formed by directly spreading the lipid solution (1 mM) in a mixture of chloroform and methanol (3:1) onto the subphase. The lipid monolayer was equilibrated until a constant surface pressure of ~20 mN m^{-1} was detected. Protein measurements were performed by careful injection of the concentrated protein solution ($c_{\text{K-Ras4B GDP}} \approx 300\ \mu M$, $c_{\text{K-Ras4B GTP}} \approx 150-200\ \mu M$ in 20 mM Tris, 5 mM $MgCl_2$, 1 mM dithioerythritol pH 7.5; $c_{CaM} \approx 270\ \mu M$ in 10 mM Hepes, 5 mM $MgCl_2$, 150 mM NaCl, 1 mM $CaCl_2$ pH 7.4) through the lipid monolayer into the D_2O subphase to yield a final concentration of K-Ras4B and Ca^{2+}/CaM of 200 and 300 nM, respectively. Further details are given in Supporting Materials and Methods.

AFM

The preparation of the supported lipid bilayers and the AFM setup is described in detail in Refs. (31,33) and Supporting Materials and Methods. For protein-membrane interaction studies, 800 μL of K-Ras4B (0.2 μM), CaM (0.3 μM), or K-Ras4B/CaM (0.2 μM/0.3 μM) in Tris buffer (20 mM Tris, 7 mM $MgCl_2$, 1 mM $CaCl_2$, pH 7.4) was injected into the AFM fluid cell and allowed to incubate for 1 h at room temperature. Measurements were performed on a MultiMode scanning probe microscope with a NanoScope IIIa controller (Digital Instruments (now Bruker), Santa Barbara, CA) and a J-scanner (scan size 125 μm). Images were obtained by applying the tapping mode in liquid with sharp nitride lever probes mounted in a fluid cell (MTFML, both from Veeco (now Bruker), Mannheim, Germany).

Fluorescence anisotropy

Frequency-domain fluorescence anisotropy measurements were performed at 25°C with a K2 multifrequency phase and modulation fluorometer (ISS, Champaign, IL). Dansyl-labeled CaM was excited by a 370 nm laser diode (370 ± 10 nm excitation filter) directly connected to a function generator, yielding intensity-modulated excitation light over a frequency range of 2−173 MHz at a cross-correlation frequency of 400 Hz. The dansyl emission was collected through a 400 nm long-pass filter. Fluorescence lifetime measurements were carried out in 5 mm path-length quartz cuvettes under magic-angle conditions before anisotropy experiments were conducted. Experimental data were fitted with the use of VINCI analysis software (ISS). A more detailed description of the setup, sample preparation, and data analysis is given in Supporting Materials and Methods.

RESULTS AND DISCUSSION

In the last few years, the importance of Ras localization in different compartments of the plasma membrane has become apparent and the impact of Ras clustering in distinct plasma membrane domains has been studied (34,35). There is evidence that distinct regions in cell membranes, termed rafts, may play a role in a wide range of important biological processes (35,36). Such liquid-ordered, sphingolipid- and cholesterol-enriched domains could also act as signaling platforms, coupling events outside of the cell to signal transduction pathways in its interior. The well-established anionic model raft membrane system used here consists of DOPC/DOPG/DPPC/DPPG/Chol at a molar ratio of 20:5:45:5:25 and segregates into liquid-ordered and liquid-disordered domains under ambient conditions, thus mimicking a heterogeneous plasma membrane with different degrees of membrane order (37,38). Phosphatidylglycerol is widely used as a simplified model of negatively charged phospholipids to mimic the electrostatic effects of the monovalent acidic lipids present in mammalian membranes. Previous studies on N-Ras and K-Ras4B revealed a membrane interaction behavior that was independent of the heterogeneous membrane composition (31,39,40), justifying the use of the low-melting-temperature lipid DOPC in liquid phase coexistence model systems, although DOPC is rare in mammalian membranes. Semisynthetic, fully functional, lipidated GDP- and GTP-loaded (with the GppNHp-bound state as a nonhydrolyzable GTP analog) K-Ras4B (30) has been investigated in the absence and presence of Ca^{2+}/CaM and/or anionic model raft membranes.

First, we carried out SPR experiments to test the ability of Ca^{2+}/CaM to dissociate K-Ras4B from membranes. SPR allows one to detect the binding and dissociation kinetics of proteins to and from a membrane surface in real time without any labeling by measuring changes in the resonance angle (41). The sensorgram includes a plot of the SPR signal in resonance units (1 RU = 1 pg mm^{-2}, i.e., surface coverage with protein in terms of mass protein/mm^2 surface area) against time (42,43). For Ca^{2+}-loaded CaM, no significant increase in RUs could be observed upon protein injection (Fig. 2), demonstrating that Ca^{2+}/CaM does not bind to

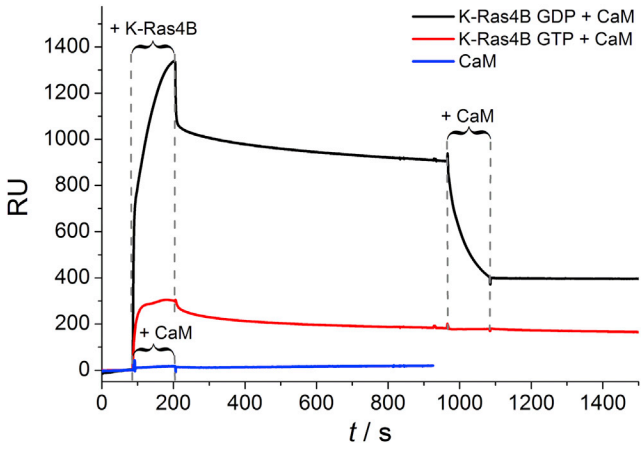

FIGURE 2 SPR sensorgrams of the binding of GDP- and GTP-loaded K-Ras4B ($c = 2\ \mu M$) to anionic lipid raft membranes and subsequent addition of Ca^{2+}/CaM ($c = 3\ \mu M$).

the immobilized membrane. The primary cause of this is repulsive interactions between the strongly negatively charged Ca^{2+}/CaM (net charge of −15 at pH 7 with four calcium ions bound; Fig. 1 *B*, *right*) and the anionic membrane. In contrast, both GDP- and GTP-bound K-Ras4B bound to anionic model raft membranes, as indicated by an increase in RUs upon protein injection (Fig. 2). Unfarnesylated K-Ras4B was used as a control and showed no significant membrane binding (Fig. S2). While changing the protein solution to buffer, we followed the dissociation of K-Ras4B from the membrane and observed amounts of quasi-irreversible bound protein of 72% and 65% for K-Ras4B GDP and K-Ras4B GTP, respectively (cf. Supporting Materials and Methods). These data are in good agreement with previous results (29). Subsequent addition of Ca^{2+}/CaM resulted in a significant decrease in RUs, i.e., a release of membrane-anchored K-Ras4B GDP. In the Ca^{2+}/CaM−K-Ras4B complex, the farnesyl anchor of K-Ras4B is buried in the hydrophobic tunnel of Ca^{2+}/CaM. This prevents membrane binding of K-Ras4B, which requires insertion of its farnesyl anchor into the membrane. However, no such marked effect could be detected for active K-Ras4B (Fig. 2). By comparison, no membrane extraction was detected for either active or inactive K-Ras4B by PDEδ in a previous study (29), and in contrast to Ca^{2+}/CaM, PDEδ itself exhibited a relatively strong affinity for heterogeneous membranes.

Second, by simultaneously recording IRRA spectra and surface pressure/time (π/t) isotherms, we studied the interaction of K-Ras4B and Ca^{2+}/CaM with anionic lipid raft monolayers. In IRRAS, the slow kinetics of K-Ras distribution in the aqueous subphase is based on the absence of convection, so the process of K-Ras diffusion to the lipid interface is rather slow. Although these interaction processes occur on much faster timescales in vivo (which of course is due to different dynamics in the complex biological cell), the underlying biophysical mechanism will not be influenced by the different dynamics. Owing to the much slower process of diffusion to the lipid interface, even kinetic intermediates may be resolved by IRRAS. The long-term stability and integrity of the pure lipid monolayer on the D_2O subphase was ensured in a control experiment (Fig. S3). Injection of the proteins underneath the lipid monolayer was accomplished at $\pi \approx 20$ mN m^{-1}. The minor changes in surface pressure together with the lack of an amide-I′ band in the corresponding IRRA spectra indicate that Ca^{2+}/CaM does not insert into the lipid monolayer. Instead, an accumulation of Ca^{2+}/CaM at the air/D_2O interface in the reference trough was detected, with the IR band around 1646 cm^{-1} being characteristic of the α-helical structure of Ca^{2+}/CaM (Fig. 3, *A* and *B*). Since this effect was not observed for membrane-binding proteins, one can assume that protein diffusion into the reference trough only occurs for non-membrane-binding proteins such as Ca^{2+}/CaM, as no accumulation of the protein at the lipid membrane is possible. Again, these results can be explained by repulsive interactions between the strongly negatively charged Ca^{2+}/CaM and the anionic membrane. By comparison, PDEδ exhibits a net charge of approximately −2 at pH 7.5. In a previous study (29), an interaction with the lipid headgroups together with a strong amide-I′ band intensity was detected for PDEδ in the IRRA spectra, indicating a parallel orientation of the β-sheets of PDEδ to the membrane interface.

Contrary to Ca^{2+}/CaM, both active and inactive K-Ras4B showed an intensive amide-I′ band in the IRRA spectra, with band maxima around 1639 cm^{-1} (Fig. 3, *D* and *C*, respectively). The corresponding π/t profiles indicate an effective insertion of the K-Ras4B farnesyl anchor into the lipid monolayer, resulting in a marked increase in surface pressure (Fig. 3 *A*). An increase of ~10 mN m^{-1} in membrane surface pressure upon injection of Ras protein is not unusual at such initial surface pressures, as we have shown previously for other Ras proteins (44). This increase results from insertion of the lipid anchors of the lipidated Ras proteins into the lipid monolayer, as nonlipidated Ras constructs are unable to insert into lipid monolayers and thus exhibit no increase in surface pressure (44). Moreover, the data presented here agree with previous studies on K-Ras4B in the presence of membranes (29,31,44). Corresponding transmission FT-IR spectroscopic measurements ensured the long-term stability of K-Ras4B proteins in the absence and presence of membranes by revealing no significant changes in secondary structure over the whole time range covered (Fig. S4) (31,45). After Ca^{2+}/CaM was injected into the D_2O subphase of the Langmuir trough containing the membrane-bound K-Ras4B proteins, a significant decrease in surface pressure was observed within ~15 min (Fig. 3 *A*), indicating a partial release of K-Ras4B from the lipid monolayer. This decrease was not due to a disturbance of the lipid monolayer during protein injection, since no such decrease was detected when solutions of proteins that have been shown to not interact with

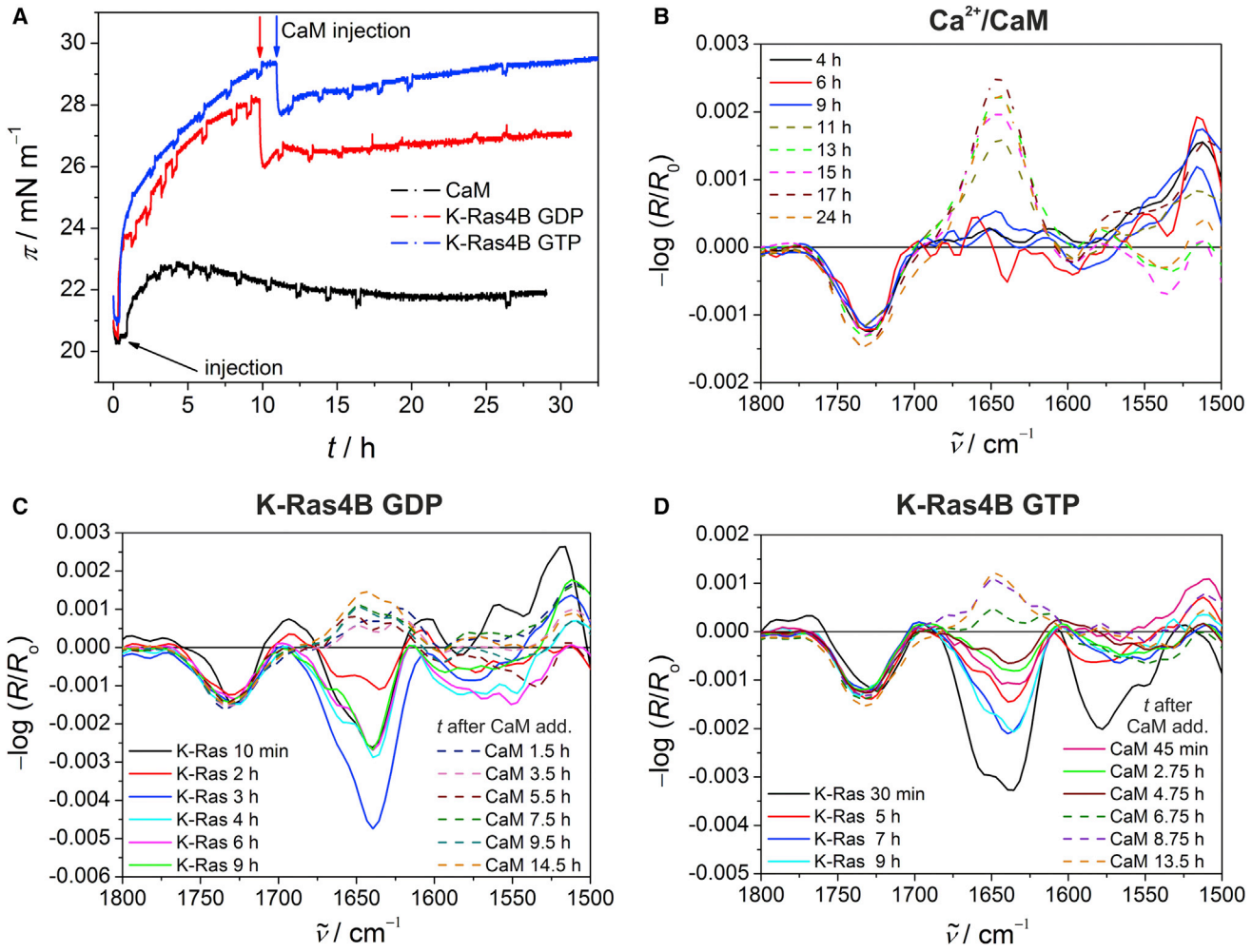

FIGURE 3 (*A*) Surface pressure profiles for K-Ras4B GDP, K-Ras4B GTP, and Ca^{2+}/CaM upon interaction with the anionic lipid raft monolayer. After equilibration of the pure lipid monolayer, i.e., observation of a stable surface pressure of ~20 mN m^{-1}, injection of K-Ras4B and CaM alone was carried out at $t = 0$ h (indicated by *black arrow*). For GDP- and GTP-loaded K-Ras4B, a concentrated solution of Ca^{2+}/CaM was injected into the D_2O subphase after ~10 h (indicated by *red and blue arrows*, respectively), resulting in a significant decrease in surface pressure within 15 min for both GDP- and GTP-loaded K-Ras4B. (*B–D*) Corresponding IRRA spectra for Ca^{2+}/CaM (*B*), K-Ras4B GDP (*C*), and K-Ras4B GTP (*D*) inserted into or adsorbed at the anionic lipid raft monolayer (with an initial surface pressure of ~20 mN m^{-1}) were acquired with p-polarized light at an angle of incidence of 35°. On the left-hand side in (*C*) and (*D*), the legend for binding of K-Ras4B to the lipid monolayer is given in a time-dependent manner up to 9 h after addition of K-Ras4B to the lipid monolayer. After ~10 h, CaM was injected into the D_2O subphase of the Langmuir trough. The legend for the spectra collected after the addition of CaM to the membrane-bound K-Ras4B is given on the right. The dashed lines indicate an accumulation of proteins at the air/D_2O interface in the reference trough.

the lipid membrane were injected into the subphase underneath the lipid monolayer (44). In contrast to the surface pressure profiles, the intensity changes in the IRRA spectra are not caused only by varying concentrations of protein at the D_2O/lipid interface. Since no changes in secondary structure take place for K-Ras4B upon membrane binding (31), contributions from orientational changes of the protein at the lipid interface are observed in the IRRA spectra. Moreover, the possibility that an accumulation of Ca^{2+}/CaM in the reference trough modulates the IRRA spectra intensity of membrane-bound K-Ras4B cannot be ruled out. Hence, it is not possible to quantitatively interpret the intensity changes of the IRRAS amide-I′ band in terms of a decreased localization of K-Ras4B at the lipid monolayer. However, since the structures of the two proteins are quite different (predominantly α-helical for Ca^{2+}/CaM and mixed α/β-type for K-Ras4B), the IR signatures for the two proteins are rather distinct. Thus, the broader amide-I′ band in the IRRA spectra of the reference trough after Ca^{2+}/CaM addition to membrane-bound K-Ras4B (*dashed lines* in Fig. 3, *C* and *D*) as compared with Ca^{2+}/CaM alone (Fig. 3 *B*), together with the disappearance of the amide-I′ band in the IRRA spectra of K-Ras4B at the lipid interface, points to a partial extraction of membrane-bound K-Ras4B from the lipid monolayer by Ca^{2+}/CaM independently of nucleotide loading (Fig. 3, *C* and *D*),

supporting the surface pressure results. In line with the electrostatic-repulsion model, binding of the strongly negatively charged Ca^{2+}/CaM to the polybasic stretch of membrane-bound K-Ras4B would reverse its charge, leading to repulsion of the complex from anionic lipid monolayers and, in this case, diffusion of the K-Ras4B−Ca^{2+}/CaM complex into the subphase and an accumulation at the air/D_2O interface (*dashed lines* in Fig. 3, *C* and *D*). The observed delay in IR spectral changes as compared with the fast change in surface pressure upon Ca^{2+}/CaM addition is due to the different timescales of data acquisition (i.e., ~1 s for π and ~40 min for IR spectra). Moreover, the slightly different timescales for K-Ras4B extraction might be caused by the different orientational flexibilities of GDP- and GTP-loaded K-Ras4B at the lipid membrane, which might modulate their initial interaction with Ca^{2+}/CaM. We previously showed that membrane-bound K-Ras4B GDP adopts a rather fixed conformation at the membrane as compared with K-Ras4B GTP, which displays a much higher orientational flexibility (44). In contrast, the previous study with PDEδ (29) revealed a dissociation of the K-Ras4B−PDEδ complex in the presence of anionic monolayers, since the π profiles and IRRA spectra of the complex resembled those of the GDP- and GTP-loaded K-Ras4B membrane interaction.

Third, we performed fluorescence anisotropy measurements to unambiguously determine whether or not Ca^{2+}/CaM can release membrane-bound K-Ras4B in a GTP-dependent manner. Preceding lifetime experiments of dansyl-labeled Ca^{2+}/CaM in buffer revealed a fluorescence lifetime of 15.9 ± 0.4 ns (cf. Supporting Materials and Methods; Fig. S5; Table S1) in accordance with published data (46). Subsequent anisotropy measurements identified an overall rotational correlation time, θ, of 9.4 ± 0.9 ns for Ca^{2+}/CaM in buffer (Fig. S6; Table S2), in agreement with earlier studies (47,48). Addition of lipid vesicles did not significantly affect $\theta_{\text{dansyl-CaM}}$, which verifies the SPR and IRRAS results in showing no membrane binding of the acidic Ca^{2+}/CaM (Fig. 4; Table S2). Since the global rotational motion of Ca^{2+}/CaM is sensitive to the overall dimensions of the protein, complex formation with K-Ras4B is expected to lead to a considerable increase in $\theta_{\text{dansyl-CaM}}$. This is confirmed by a detected overall rotational correlation time of 17.9 and 16.1 ns for Ca^{2+}/CaM in complex with GDP- and GTP-loaded K-Ras4B, respectively, in solution. Further addition of lipid vesicles to the complex did not alter the rotational dynamics of Ca^{2+}/CaM. Consequently, Ca^{2+}/CaM binds to K-Ras4B in the absence and presence of membranes irrespective of nucleotide loading. Moreover, no membrane binding was detected for Ca^{2+}/CaM-complexed K-Ras4B, since this would result in a marked increase in $\theta_{\text{dansyl-CaM}}$, as shown in a previous study of K-Ras4B (29). Moreover, the Ca^{2+}/CaM−K-Ras4B complex was stable in the presence of anionic membranes, because complex dissociation would result in the value detected for $\theta_{\text{dansyl-CaM}}$ in buffer. This result is in contrast to previously published data for PDEδ, which pointed to a dissociation of the K-Ras4B−PDEδ complex upon membrane interaction (29).

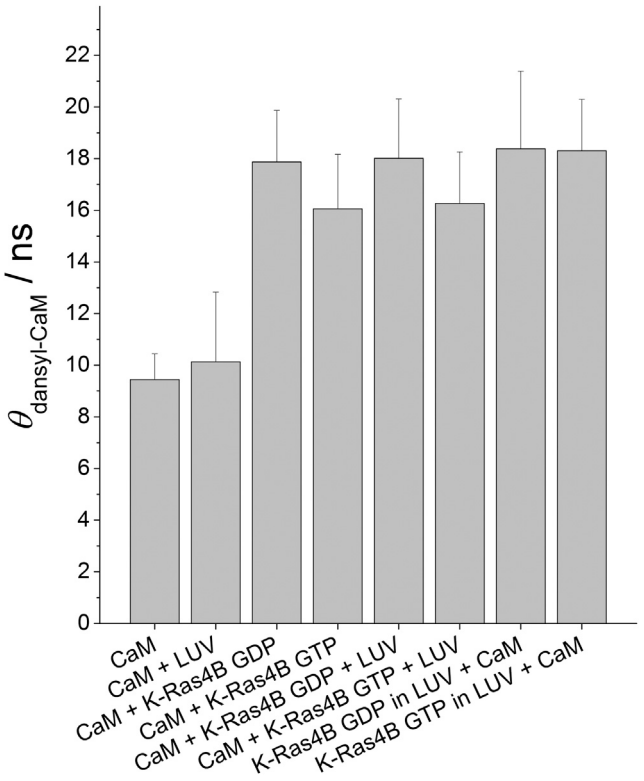

FIGURE 4 Overall rotational correlation times of dansyl-labeled Ca^{2+}/CaM at $T = 25°C$. Results are shown for Ca^{2+}/CaM in the presence and absence of GDP- and GTP-loaded K-Ras4B and/or anionic model raft membranes (lipid/K-Ras4B ratio of 200:1). The underlying fitting parameters are given in Tables S1 and S2.

To verify a direct release of membrane-bound K-Ras4B by Ca^{2+}/CaM, K-Ras4B was incubated with lipid vesicles followed by subsequent addition of Ca^{2+}/CaM. Previous results confirmed stable membrane binding of K-Ras4B under these conditions (29,49). Rotational correlation times of 15 ns and 25 ns were determined for BODIPY-labeled K-Ras4B GDP in the absence and presence of membranes, respectively. To verify that the change in θ was indeed due to the binding of K-Ras4B to large unilamellar vesicles, we performed the same experiment with unlipidated K-Ras4B, which showed a rotational correlation time of 13 ns, i.e., no membrane binding (29,49). Once bound, K-Ras4B is known to be stably anchored in the membrane (31). The value of $\theta_{\text{dansyl-CaM}} = 18.3$ ns determined here for both K-Ras4B GDP and GTP shows that Ca^{2+}/CaM is able to bind to membrane-anchored K-Ras4B and extract it from anionic membranes irrespective of GDP/GTP (Fig. 4; Table S2).

Finally, to gain complementary spatial information on the single-molecule level, we carried out time-lapse AFM

experiments. Protein-enriched domains were observed within the bulk liquid-disordered phase for both GDP- and GTP-bound K-Ras4B, in agreement with previous data that focused on the membrane localization of K-Ras4B (29,31). Corresponding AFM images of the anionic raft membrane before and after addition of K-Ras4B are given in Figs. S7 and S8 (cf. Supporting Results). Due to electrostatic repulsion, Ca^{2+}/CaM itself showed no significant membrane binding (Fig. S9). However, upon addition of Ca^{2+}/CaM to membrane-bound K-Ras4B, no substantial changes were detected (Fig. S8). This may be due to the large K-Ras4B clusters observed in the AFM images, which may restrict efficient binding of Ca^{2+}/CaM to membrane-anchored K-Ras4B and thus impede K-Ras4B membrane extraction. Moreover, steric constraints could be induced by the small separation of the lipid bilayer and solid support, which might impede the displacement of proteins. When the preformed K-Ras4B−Ca^{2+}/CaM complex was added to anionic membranes, the AFM images showed a considerably lower amount of K-Ras4B clusters. This indicates that Ca^{2+}/CaM is able to bind K-Ras4B in solution and obstructs binding of K-Ras4B to the membrane independently of its nucleotide state (Fig. S9). Again, in the previous study (29), addition of the K-Ras4B−PDEδ complex to anionic membranes led to AFM images that mirrored the membrane partitioning behavior of the single components, arguing for a dissociation of the complex.

CONCLUSIONS

Taken together, the IRRAS and fluorescence anisotropy data clearly demonstrate that Ca^{2+}/CaM binds to membrane-anchored K-Ras4B and dissociates it from negatively charged membranes in a nucleotide-independent manner. In line with the electrostatic repulsion model, binding of the strongly negatively charged Ca^{2+}/CaM to the polybasic stretch of K-Ras4B would reverse its charge, leading to repulsion of the complex from membranes containing anionic lipids. One farnesyl anchor alone is not sufficient to stably anchor Ras proteins in membranes. The combined data also reveal no binding of the K-Ras4B−Ca^{2+}/CaM complex to anionic membranes, which can be easily explained by the farnesyl anchor buried in the hydrophobic pocket of Ca^{2+}/CaM and repulsive electrostatic interactions, according to the model described above. This leads to the important conclusion that plasma membrane binding of K-Ras4B would not be possible in the CaM-complexed state. This would imply that binding of Ca^{2+}/CaM to K-Ras4B inhibits its activity and thus signaling to Ras effectors (e.g., Raf) in vivo and consequently also ERK1/2 activation, since K-Ras4B membrane association is crucial for its function. Therefore, Ca^{2+}/CaM would function as a negative regulator of K-Ras4B signaling in intact cells by releasing K-Ras4B from negatively charged membranes and preventing its plasma membrane localization. This is in agreement with previous results, which showed that Ca^{2+}/CaM plays an essential role in the downregulation of the Ras/Raf/MEK/ERK pathway in cultured fibroblasts (50) and that inactivation of CaM enables activation of K-Ras4B (16). Thus, Ca^{2+}/CaM seems to be an important element in the differential downregulation of Ras, since Ca^{2+}/CaM binds specifically to K-Ras4B (but not N-Ras, K-Ras4A, or H-Ras) (16). Moreover, the polybasic-prenyl motif of K-Ras4B has been reported to act as a reversible Ca^{2+}/CaM-regulated molecular switch that removes K-Ras4B from the plasma membrane and partially redistributes it to internal sites in neurons (15). Finally, a very recent study (51) revealed that binding of K-Ras to CaM leads to a sustained suppression of Wnt/Ca^{2+} signaling, which causes increased tumorigenicity. The authors of that study suggested that blocking of this Ras isoform-specific CaM interaction might represent a novel approach for selective K-Ras targeting.

A mechanism similar to that observed for the interaction of Ca^{2+}/CaM with K-Ras4B has been detected for the binding of Ca^{2+}/CaM to the myristoylated alanine-rich C-kinase substrate (MARCKS). Again, since one myristate anchor cannot hold the protein on the membrane, the binding of Ca^{2+}/CaM to the central region of the basic cluster of MARCKS is expected to repel the complex from the membrane, thus leading to translocation of MARCKS from the plasma membrane to the cytoplasm (52,53).

The reason for the discrepancies between the SPR data, that revealed membrane extraction by Ca^{2+}/CaM only for K-Ras4B GDP, and the rest of the data, which showed no nucleotide dependency, most likely lies in the different extents of clustering for GDP- and GTP-loaded K-Ras4B in immobilized membranes. Protein clustering is more pronounced for the active form of Ras in supported bilayers, as seen in corresponding AFM experiments for both K-Ras and N-Ras (31,33). Therefore, steric constraints introduced by strong clustering are a very likely reason for the observed nucleotide dependence of Ca^{2+}/CaM binding to membrane-bound K-Ras4B in SPR. In IRRAS and fluorescence anisotropy experiments, no solid support is used for membrane immobilization (corresponding to a higher lateral mobility of the lipids at the air/D_2O interface in IRRAS experiments and in freestanding lipid vesicles in anisotropy experiments). Therefore, the lack of significant extraction of membrane-bound K-Ras4B by Ca^{2+}/CaM as detected by AFM is most probably due to the large K-Ras4B clusters observed in the AFM images, which restrict efficient binding of Ca^{2+}/CaM to K-Ras4B bound to solid-supported membranes and thus largely impede K-Ras4B membrane extraction. Moreover, steric constraints could be induced by the small separation of the immobilized lipid bilayer and solid support (~0.5−2.0 nm in buffer solution), which might impede easy displacement of proteins. Since Ras nanoclusters are thought to be much smaller in vivo (34) as compared with the strong clustering

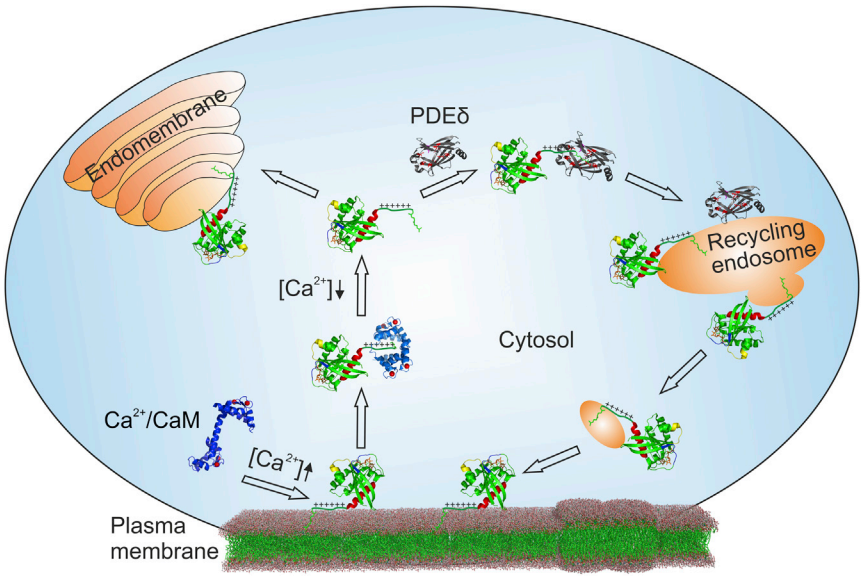

FIGURE 5 Schematic illustration of the PDEδ and Ca^{2+}/CaM-modulated K-Ras4B localization cycle. Ca^{2+}/CaM extracts K-Ras4B from the plasma membrane at elevated levels of intracellular free Ca^{2+}. This process might be facilitated by a decrease of the most-negative plasma membrane's surface charge upon an increase in cytosolic Ca^{2+}. After cell stimulation, the free Ca^{2+} concentration, $[Ca^{2+}]$, decreases, leading to a dissociation of the Ca^{2+}/CaM−K-Ras4B complex. In the cytosol, K-Ras4B can bind to endomembranes or PDEδ, with the latter solubilizing K-Ras4B and facilitating cytoplasmic diffusion. When the PDEδ/K-Ras4B complex reaches the negatively charged recycling endosome, K-Ras4B can be released and its farnesyl anchor can be inserted into the membrane. Taking into account recent results from Schmick et al. (54), one can envisage a directed vesicular transport that brings K-Ras4B back to the plasma membrane, where it clusters in less-ordered domains.

in microdomains observed in experiments using immobilized membranes, we conclude that membrane extraction by Ca^{2+}/CaM occurs independently of GTP loading, as seen in the IRRAS and fluorescence anisotropy experiments presented here.

Contrary to the previously analyzed PDEδ, the Ca^{2+}/CaM−K-Ras4B complex turned out to be stable in the presence of anionic membranes. In a recent study (29), we showed that PDEδ is unable to extract K-Ras4B from heterogeneous model membranes irrespective of GTP loading. The enhanced affinity of the K-Ras4B−PDEδ complex particularly for anionic membranes, together with the observation that K-Ras4B is released from PDEδ upon membrane interaction, led us to propose an effective delivery of PDEδ-solubilized K-Ras4B to the plasma membrane. This is in accordance with findings by Schmick et al. (13), which showed that binding of K-Ras4B to PDEδ involves a passive sequestration in the cytoplasm of dissociated K-Ras4B from any membrane.

By taking into account recent insights into the dynamic, spatially organizing cycle of Ras (54), one can envisage that PDEδ and Ca^{2+}/CaM jointly control K-Ras4B plasma membrane localization, with Ca^{2+}/CaM playing a different part than PDEδ in the regulation of K-Ras4B membrane binding (Fig. 5). Since the signaling activity of K-Ras4B is intrinsically tied to its level of enrichment at the plasma membrane, interference in K-Ras4B plasma membrane localization would constitute a possible means to impact cell growth and counter oncogenic K-Ras4B signaling.

SUPPORTING MATERIAL

Supporting Materials and Methods, Supporting Results, nine figures, and two tables are available at http://www.biophysj.org/biophysj/supplemental/S0006-3495(16)30389-7.

AUTHOR CONTRIBUTIONS

R.W. and K.W. designed research; B.S., S.K., and K.W. performed research and analyzed data; H.W. contributed reagents/analytic tools; and B.S., S.K., R.W., and K.W. wrote the article.

ACKNOWLEDGMENTS

We thank Simone Möbitz for labeling of CaM and initial SPR experiments, Sasikala Thavam for help with the lipopeptide synthesis, Christine Nowak for technical assistance with Ras protein expression and ligation, and Andrea Gohlke for initial SPR experiments. We also thank Stefan M. Kast and Florian Mrugalla for providing Fig. S1 and helpful discussion.

This research was supported by the Deutsche Forschungsgemeinschaft (SFB 642).

SUPPORTING CITATIONS

References (55–57) appear in the Supporting Material.

REFERENCES

1. Barbacid, M. 1987. ras genes. *Annu. Rev. Biochem.* 56:779–827.
2. Hancock, J. F. 2003. Ras proteins: different signals from different locations. *Nat. Rev. Mol. Cell Biol.* 4:373–384.
3. Wittinghofer, A., and H. Waldmann. 2000. Ras—a molecular switch involved in tumor formation. *Angew. Chem. Int. Ed. Engl.* 39:4192–4214.
4. Wittinghofer, A., and E. F. Pai. 1991. The structure of Ras protein: a model for a universal molecular switch. *Trends Biochem. Sci.* 16:382–387.
5. Friday, B. B., and A. A. Adjei. 2005. K-ras as a target for cancer therapy. *Biochim. Biophys. Acta.* 1756:127–144.
6. Bos, J. L. 1989. ras oncogenes in human cancer: a review. *Cancer Res.* 49:4682–4689.
7. Prior, I. A., P. D. Lewis, and C. Mattos. 2012. A comprehensive survey of Ras mutations in cancer. *Cancer Res.* 72:2457–2467.

8. Hancock, J. F., H. Paterson, and C. J. Marshall. 1990. A polybasic domain or palmitoylation is required in addition to the CAAX motif to localize p21ras to the plasma membrane. *Cell.* 63:133–139.
9. Jackson, J. H., J. W. Li, …, C. G. Cochrane. 1994. Polylysine domain of K-ras 4B protein is crucial for malignant transformation. *Proc. Natl. Acad. Sci. USA.* 91:12730–12734.
10. Marshall, C. J. 1996. Ras effectors. *Curr. Opin. Cell Biol.* 8:197–204.
11. Willumsen, B. M., A. Christensen, …, D. R. Lowy. 1984. The p21 ras C-terminus is required for transformation and membrane association. *Nature.* 310:583–586.
12. Chandra, A., H. E. Grecco, …, P. I. Bastiaens. 2011. The GDI-like solubilizing factor PDEδ sustains the spatial organization and signalling of Ras family proteins. *Nat. Cell Biol.* 14:148–158.
13. Schmick, M., N. Vartak, …, P. I. Bastiaens. 2014. KRas localizes to the plasma membrane by spatial cycles of solubilization, trapping and vesicular transport. *Cell.* 157:459–471.
14. Ismail, S. A., Y. X. Chen, …, A. Wittinghofer. 2011. Arl2-GTP and Arl3-GTP regulate a GDI-like transport system for farnesylated cargo. *Nat. Chem. Biol.* 7:942–949.
15. Fivaz, M., and T. Meyer. 2005. Reversible intracellular translocation of KRas but not HRas in hippocampal neurons regulated by Ca^{2+}/calmodulin. *J. Cell Biol.* 170:429–441.
16. Villalonga, P., C. López-Alcalá, …, N. Agell. 2001. Calmodulin binds to K-Ras, but not to H- or N-Ras, and modulates its downstream signaling. *Mol. Cell. Biol.* 21:7345–7354.
17. Abraham, S. J., R. P. Nolet, …, V. Gaponenko. 2009. The hypervariable region of K-Ras4B is responsible for its specific interactions with calmodulin. *Biochemistry.* 48:7575–7583.
18. Crivici, A., and M. Ikura. 1995. Molecular and structural basis of target recognition by calmodulin. *Annu. Rev. Biophys. Biomol. Struct.* 24:85–116.
19. Klee, C. B., and T. C. Vanaman. 1982. Calmodulin. *Adv. Protein Chem.* 35:213–321.
20. Babu, Y. S., C. E. Bugg, and W. J. Cook. 1988. Structure of calmodulin refined at 2.2 A resolution. *J. Mol. Biol.* 204:191–204.
21. Zhang, M., T. Tanaka, and M. Ikura. 1995. Calcium-induced conformational transition revealed by the solution structure of apo calmodulin. *Nat. Struct. Biol.* 2:758–767.
22. Vetter, S. W., and E. Leclerc. 2003. Novel aspects of calmodulin target recognition and activation. *Eur. J. Biochem.* 270:404–414.
23. Hoeflich, K. P., and M. Ikura. 2002. Calmodulin in action: diversity in target recognition and activation mechanisms. *Cell.* 108:739–742.
24. Matsubara, M., T. Nakatsu, …, H. Taniguchi. 2004. Crystal structure of a myristoylated CAP-23/NAP-22 N-terminal domain complexed with Ca^{2+}/calmodulin. *EMBO J.* 23:712–718.
25. Sidhu, R. S., R. R. Clough, and R. P. Bhullar. 2003. Ca^{2+}/calmodulin binds and dissociates K-RasB from membrane. *Biochem. Biophys. Res. Commun.* 304:655–660.
26. Bhagatji, P., R. Leventis, …, J. R. Silvius. 2010. Multiple cellular proteins modulate the dynamics of K-ras association with the plasma membrane. *Biophys. J.* 99:3327–3335.
27. Wu, L. J., L. R. Xu, …, Y. Liang. 2011. Both the C-terminal polylysine region and the farnesylation of K-RasB are important for its specific interaction with calmodulin. *PLoS One.* 6:e21929.
28. Lopez-Alcalá, C., B. Alvarez-Moya, …, N. Agell. 2008. Identification of essential interacting elements in K-Ras/calmodulin binding and its role in K-Ras localization. *J. Biol. Chem.* 283:10621–10631.
29. Weise, K., S. Kapoor, …, R. Winter. 2012. Dissociation of the K-Ras4B/PDEδ complex upon contact with lipid membranes: membrane delivery instead of extraction. *J. Am. Chem. Soc.* 134:11503–11510.
30. Chen, Y. X., S. Koch, …, H. Waldmann. 2010. Synthesis of the Rheb and K-Ras4B GTPases. *Angew. Chem. Int. Ed. Engl.* 49:6090–6095.
31. Weise, K., S. Kapoor, …, R. Winter. 2011. Membrane-mediated induction and sorting of K-Ras microdomain signaling platforms. *J. Am. Chem. Soc.* 133:880–887.
32. Gohlke, A., G. Triola, …, R. Winter. 2010. Influence of the lipid anchor motif of N-ras on the interaction with lipid membranes: a surface plasmon resonance study. *Biophys. J.* 98:2226–2235.
33. Weise, K., G. Triola, …, R. Winter. 2009. Influence of the lipidation motif on the partitioning and association of N-Ras in model membrane subdomains. *J. Am. Chem. Soc.* 131:1557–1564.
34. Plowman, S. J., C. Muncke, …, J. F. Hancock. 2005. H-ras, K-ras, and inner plasma membrane raft proteins operate in nanoclusters with differential dependence on the actin cytoskeleton. *Proc. Natl. Acad. Sci. USA.* 102:15500–15505.
35. Omerovic, J., and I. A. Prior. 2009. Compartmentalized signalling: Ras proteins and signalling nanoclusters. *FEBS J.* 276:1817–1825.
36. Simons, K., and D. Toomre. 2000. Lipid rafts and signal transduction. *Nat. Rev. Mol. Cell Biol.* 1:31–39.
37. Kapoor, S., A. Werkmüller, …, R. Winter. 2011. Temperature-pressure phase diagram of a heterogeneous anionic model biomembrane system: results from a combined calorimetry, spectroscopy and microscopy study. *Biochim. Biophys. Acta.* 1808:1187–1195.
38. Evers, F., C. Jeworrek, …, R. Winter. 2012. Detection of lipid raft domains in neutral and anionic Langmuir monolayers and bilayers of complex lipid composition. *Soft Matter.* 8:2170–2175.
39. Vogel, A., J. Nikolaus, …, D. Huster. 2014. Interaction of the human N-Ras protein with lipid raft model membranes of varying degrees of complexity. *Biol. Chem.* 395:779–789.
40. Vogel, A., G. Reuther, …, D. Huster. 2009. The lipid modifications of Ras that sense membrane environments and induce local enrichment. *Angew. Chem. Int. Ed. Engl.* 48:8784–8787.
41. Green, R. J., R. A. Frazier, …, S. J. Tendler. 2000. Surface plasmon resonance analysis of dynamic biological interactions with biomaterials. *Biomaterials.* 21:1823–1835.
42. Mozsolits, H., W. G. Thomas, and M. I. Aguilar. 2003. Surface plasmon resonance spectroscopy in the study of membrane-mediated cell signalling. *J. Pept. Sci.* 9:77–89.
43. Besenicar, M., P. Macek, …, G. Anderluh. 2006. Surface plasmon resonance in protein-membrane interactions. *Chem. Phys. Lipids.* 141:169–178.
44. Kapoor, S., K. Weise, …, R. Winter. 2012. The role of G-domain orientation and nucleotide state on the Ras isoform-specific membrane interaction. *Eur. Biophys. J.* 41:801–813.
45. Kapoor, S., G. Triola, …, R. Winter. 2012. Revealing conformational substates of lipidated N-Ras protein by pressure modulation. *Proc. Natl. Acad. Sci. USA.* 109:460–465.
46. Kincaid, R. L., M. Vaughan, …, V. A. Tkachuk. 1982. Ca^{2+}-dependent interaction of 5-dimethylaminonaphthalene-1-sulfonyl-calmodulin with cyclic nucleotide phosphodiesterase, calcineurin, and troponin I. *J. Biol. Chem.* 257:10638–10643.
47. Yao, Y., C. Schöneich, and T. C. Squier. 1994. Resolution of structural changes associated with calcium activation of calmodulin using frequency domain fluorescence spectroscopy. *Biochemistry.* 33:7797–7810.
48. Anderson, S. R. 1991. Time-resolved fluorescence spectroscopy. Applications to calmodulin. *J. Biol. Chem.* 266:11405–11408.
49. Werkmüller, A., G. Triola, …, R. Winter. 2013. Rotational and translational dynamics of ras proteins upon binding to model membrane systems. *ChemPhysChem.* 14:3698–3705.
50. Bosch, M., J. Gil, …, N. Agell. 1998. Calmodulin inhibitor W13 induces sustained activation of ERK2 and expression of p21(cip1). *J. Biol. Chem.* 273:22145–22150.

51. Wang, M. T., M. Holderfield, …, F. McCormick. 2015. K-ras promotes tumorigenicity through suppression of non-canonical Wnt signaling. *Cell.* 163:1237–1251.

52. Kim, J., T. Shishido, …, S. McLaughlin. 1994. Phosphorylation, high ionic strength, and calmodulin reverse the binding of MARCKS to phospholipid vesicles. *J. Biol. Chem.* 269:28214–28219.

53. McLaughlin, S., and D. Murray. 2005. Plasma membrane phosphoinositide organization by protein electrostatics. *Nature.* 438:605–611.

54. Schmick, M., A. Kraemer, and P. I. H. Bastiaens. 2015. Ras moves to stay in place. *Trends Cell Biol.* 25:190–197.

55. Gratton, E., and M. Limkeman. 1983. A continuously variable frequency cross-correlation phase fluorometer with picosecond resolution. *Biophys. J.* 44:315–324.

56. Gratton, E., D. M. Jameson, and R. D. Hall. 1984. Multifrequency phase and modulation fluorometry. *Annu. Rev. Biophys. Bioeng.* 13:105–124.

57. Humphrey, W., A. Dalke, and K. Schulten. 1996. VMD: visual molecular dynamics. *J. Mol. Graph.* 14:33–38.

58. Baker, N. A., D. Sept, …, J. A. McCammon. 2001. Electrostatics of nanosystems: application to microtubules and the ribosome. *Proc. Natl. Acad. Sci. USA.* 98:10037–10041.

Biophysical Journal, Volume *111*

Supplemental Information

Regulation of K-Ras4B Membrane Binding by Calmodulin

Benjamin Sperlich, Shobhna Kapoor, Herbert Waldmann, Roland Winter, and Katrin Weise

MATERIALS AND METHODS

Sample preparation

Stock solutions of 10 mg mL^{-1} lipid (DOPC, DOPG, DPPG, DPPC, Chol) in chloroform/methanol 4:1 for DPPG and chloroform for all other lipids were prepared and mixed to obtain 1.94 mg of total lipid with the composition of DOPC/DOPG/DPPC/DPPG/Chol 20:5:45:5:25 (mol%). The majority of the chloroform was evaporated with a nitrogen stream and all solvent was subsequently removed by drying under vacuum overnight. All buffers were filtered through filters of 0.02 µm pore size (Whatman, Dassel, Germany) before use. The dry lipid film was resuspended with 1 mL of 10 mM Hepes, 5 mM $MgCl_2$, 150 mM NaCl, 1 mM $CaCl_2$, pH 7.4 for the SPR or 20 mM Tris, 7 mM $MgCl_2$, 1 mM $CaCl_2$, pH 7.4 for the AFM and fluorescence spectroscopy experiments to yield a total lipid concentration of 3 mM. Afterwards, the lipid mixture was vortexed, kept in a water bath at 65 °C for 15 min, and sonicated for 10 min. After five freeze-thaw-vortex cycles and brief sonication, large multilamellar vesicles were formed and transformed to large unilamellar vesicles (LUVs) of uniform size by use of an extruder (Avanti Polar Lipids, Alabaster, USA) with polycarbonate membranes of 100 nm pore size at 65 °C (1,2). The extruded lipid solution was further diluted to a concentration of 0.5 mM for SPR experiments.

Atomic force microscopy

Vesicle fusion on mica was carried out by depositing 35 µL of the extruded lipid vesicle solution together with 35 µL of Tris buffer (20 mM Tris, 7 mM $MgCl_2$, 1 mM $CaCl_2$, pH 7.4) on freshly cleaved mica (NanoAndMore, Wetzlar, Germany) and incubation in a wet chamber at 70 °C for 2 h. After vesicle fusion, the samples were rinsed carefully with Tris buffer to remove excess unspread lipid vesicles (1,2). For the protein–membrane interaction studies, 800 µL of either K-Ras4B ($c_{K\text{-}Ras4B}$ = 0.2 µM), calmodulin (c_{CaM} = 0.3 µM) or K-Ras4B–Ca^{2+}/CaM (0.2 µM / 0.3 µM) in Tris buffer were slowly injected into the AFM fluid cell and allowed to incubate for 1 h at room temperature. Afterwards, the AFM fluid cell was rinsed carefully with Tris buffer to remove unbound protein. Measurements were performed at room temperature on a MultiMode scanning probe microscope with a NanoScope IIIa controller (Digital Instruments (now Bruker), Santa Barbara, CA, USA) and usage of a J-Scanner (scan size 125 µm). Images were obtained by applying the tapping mode in liquid with sharp nitride lever (SNL) probes mounted in an AFM fluid cell (MTFML, both Veeco (now Bruker), Mannheim, Germany). Tips with nominal force constants of 0.24 N m^{-1} were used at driving frequencies around 9 kHz and drive amplitudes between 200 and 400 mV. Scan frequencies were between 1.0 Hz and 2.0 Hz. Height and phase images with resolutions of 512 × 512 pixels were analyzed using the image analysis and processing software NanoScope version 5 and 6 (Veeco (now Bruker), Mannheim, Germany) and Origin 8.6 (OriginLab, Northampton, USA).

Surface plasmon resonance

SPR experiments were carried out with a Biacore 3000 system (Biacore, Uppsala, Sweden; now GE Healthcare, Freiburg, Germany). For the protein-membrane interaction studies, the L1 sensor chip (GE Healthcare, Freiburg, Germany) was used, which is composed of a thin lipophilic modified dextran matrix on a gold surface, upon which lipid bilayers can be immobilized through the capture of liposomes by the lipophilic compounds. The chip has been shown to be suitable for the generation of model membrane systems that provide a flexible lipid bilayer surface that closely resembles the surface of a cellular membrane. All measurements were carried out at a temperature of 25 °C, with the samples cooled at 10 °C in the autosampler before the measurements were started. Prior to the experiment, the L1 chip was primed 4× with Hepes buffer (10 mM Hepes, 5 mM $MgCl_2$, 150 mM NaCl, 1 mM $CaCl_2$, pH 7.4). Afterwards, the chip surface underwent a cleaning program by injecting

30 μL 2-propanol / 50 mM NaOH (2:3), 10 μL octyl β-D-glucopyranoside (40 mM), and 30 μL Chaps (20 mM), NaCl (100 mM), and $CaCl_2$ (20 mM) at a flow rate of 5 μL/min. For the vesicle immobilization, 15 μL of the extruded lipid vesicle solution (0.5 mM) were injected twice at a flow rate of 2 μL/min, which was followed by a stabilization phase by injecting 50 μL of Hepes buffer at a flow rate of 100 μL/min and three further injections of 10 μL 25 mM NaOH at a flow rate of 5 μL/min. Finally, the lipid surface was stabilized by injecting 40 μL Hepes buffer at a flow rate of 20 μL/min. After baseline stabilization, 40 μL of the protein containing solution ($c_{\text{K-Ras4B}}$ = 2 μM, c_{CaM} = 3 μM) were injected at a flow rate of 20 μL/min and the dissociation was followed for 30 min. Next the chip surface was regenerated using the cleaning program. The degree of chip surface coverage with lipids was determined by means of 0.5 μM BSA and was found to be ≥75% for all cases. To eliminate unspecific binding effects such as the interaction of Hepes buffer with the L1 chip and nonspecific binding of the proteins to the pure L1 chip that depend on the determined lipid coverage, these signals were subtracted from the actual sensorgrams of the respective protein solutions. Hence, the ratio of the maximal amplitude of the BSA-membrane and BSA-chip sensorgram yields the amount of the chip surface that is not covered with lipids and is used as a factor for correcting the zeroized (i.e., setting the baseline before injection of the protein solution to zero) protein-chip sensorgram. This corrected sensorgram is then subtracted from the buffer corrected and zeroized protein-membrane sensorgram to yield the final protein-membrane sensorgram for analysis. All sensorgrams were recorded at a frequency of 10 Hz.

For all measurements performed, the SPR data were analyzed on the basis of a multi-step model owing to the non-simple-exponential association and dissociation curves observed in the sensorgrams for the protein-membrane interaction, reflecting a complex interaction behavior. A two-step reaction model was shown to provide an appropriate curve-fitting algorithm and describes a process with two reaction steps that, in terms of protein-lipid interactions, correspond to:

$$\mathrm{P} + \mathrm{L} \underset{k_{\text{off},1}}{\overset{k_{\text{on},1}}{\rightleftharpoons}} \mathrm{PL} \underset{k_{\text{off},2}}{\overset{k_{\text{on},2}}{\rightleftharpoons}} \mathrm{PL}^{*} \qquad \text{(Scheme S1)}$$

where the soluble protein (P) binds to the immobilized lipids (L) forming a primary binding complex (PL) and a secondary protein-lipid complex (PL*, e.g. a clustered state as shown for K-Ras4B by atomic force microscopy) after relocation of protein and lipid molecules within the lipid bilayer plane. The effect of the K-Ras4B clustering on the response measured is indirect in altering the equilibrium between the bound and free forms of the protein, allowing a dissociation of PL* only through reversal of the clustering reaction step. To directly obtain values for the association rate constant k_{on}, the whole sensorgram was fitted to the two-step model. Curve fitting was performed by using the Marquardt-Levenberg algorithm and the fitted curves were generated by numerical integration of the differential equations that describe the reaction scheme. This fitting procedure was implemented in the BIAevaluation software 4.1 (Biacore, Uppsala, Sweden). Whereas the two-step fit of the whole sensorgram gave reasonable results for the association phase, a larger discrepancy was observed for the fitted dissociation part of the curve. Thus, the dissociation phase was fitted separately to a biexponential model (Eq. S1) using Origin 8.6, yielding two independent dissociation rate constants $k_{\text{off},1}$ and $k_{\text{off},2}$ as well as their respective contributions A_1 and A_2.

$$R = A_1 \cdot e^{-k_{\text{off},1}(t-t_0)} + A_2 \cdot e^{-k_{\text{off},2}(t-t_0)} + \text{offset} \qquad \text{(S1)}$$

t_0 indicates the beginning of the dissociation phase, i.e., the time point when the flow cell switched from protein to buffer solution. The relative amount of quasi-irreversibly bound protein was derived by correlating the offset value of the biexponential fit to the initial amplitude at the starting point (t = 0) of the dissociation phase corresponding to the following equation:

$$\text{quasi} - \text{irrevers.} = \frac{\text{offset}}{A_1 + A_2 + \text{offset}}. \quad \text{(S2)}$$

The model and the corresponding analysis have been described in detail before (1,3).

Infrared reflection absorption spectroscopy

All experiments were performed with a Wilhelmy film balance (Riegler, Berlin, Germany) using a filter paper as Wilhelmy plate. Two teflon troughs of different sizes were linked by two small bores to ensure equal heights of the air-D_2O interface in both troughs. The temperature of the subphase was maintained at 20 ± 0.5°C and measurements were performed in the small (reference) trough at constant surface area. A Plexiglas hood covered the entire reflection attachment to minimize the evaporation of subphase. Both troughs were filled with 20 mM Tris, 7 mM $MgCl_2$, 1 mM $CaCl_2$, pD 7.4. Monolayers of DOPC/DOPG/DPPC/DPPG/Chol 20:5:45:5:25 (mol%) were formed by directly spreading the lipid solution (1 mM) in a mixture of chloroform and methanol (3:1) onto the subphase. Protein measurements were performed by injecting the concentrated protein solution into the aqueous subphase underneath the lipid monolayer to yield a final concentration of K-Ras4B and Ca^{2+}/CaM of 200 and 300 nM, respectively.

Infrared spectra were recorded using a Vertex 70 FT-IR spectrometer (Bruker, Germany) connected to an A511 reflection attachment (Bruker) with an MCT detector using the trough system described above (4). The IR beam is focused by several mirrors onto the subphase and the trough system was positioned on a movable platform to be able to shuttle between sample and reference troughs. This shuttle technique diminishes the spectral interference due to water vapour absorption in the light beam. Parallel polarized light at an angle of incidence of 35° was used for recording of the IRRA spectra. All spectra were recorded at a spectral resolution of 8 cm^{-1} using Blackman-Harris-3-term apodization and a zero filling factor of 2. For each spectrum 2000 scans were co-added. The single beam reflectance spectrum of the large trough was ratioed as background (R_o) to the single beam reflectance spectrum of the lipid monolayer on the reference trough (R) to calculate the reflection absorption spectrum as $-\log(R/R_o)$.

Transmission Fourier-Transform infrared spectroscopy

For the transmission infrared spectroscopic experiments, the dry lipid mixture was hydrated with 100 μL of 20 mM Tris, 7 mM $MgCl_2$, pD 7.4, sonicated at 70 °C for 10 min and subsequently subjected to five freeze-thaw-vortex cycles. Afterwards, unilamellar vesicles of homogeneous size were obtained by using an extruder (Avanti Polar Lipids, Alabaster, AL) with polycarbonate membranes of 100 nm pore size at 70 °C. For the protein-lipid interaction studies, the GDP- and GTP-loaded K-Ras4B protein (m = 100 μg) was lyophilized for 3 h to remove H_2O and afterwards 20 μL of the freshly extruded lipid mixture were added ($c_{K\text{-}Ras}$ = 233 μM). The FT-IR cell was then assembled and spectra collection started.

Measurements were performed at 25 °C with a Nicolet 5700 FT-IR spectrometer equipped with a liquid nitrogen cooled MCT (HgCdTe) detector and a cell with CaF_2 windows that are separated by 50 μm mylar spacers. The spectrometer was purged continuously with dry air to remove water vapor. Typically, FT-IR-spectra of 128 scans were taken with a resolution of 2 cm^{-1} and corresponding processing was performed using GRAMS software (Thermo Electron). After background subtraction, the spectra were baseline corrected and normalized by setting the area between 1700 and 1600 cm^{-1} to 1 to allow for a quantitative analysis of the time evolution of secondary structural changes.

For the analysis of the secondary structure changes, second derivative and Fourier self-deconvolution (FSD) were applied to the normalized spectra to identify the components of the amide-I′ band region. These peaks were then fitted to the normalized raw spectra using a Levenberg-Marquardt curve fitting routine with bands of Voigt line shape. All spectra were

fitted with similar set of peaks and parameters. In ambiguous cases (such as the overlap of unordered and α-helical band regions), information from NMR and X-ray diffraction was taken into account. The area under each peak represents the fraction of the respective component (assuming similar transition dipole moments for the different conformers) and was finally used to determine the percentages of the secondary structure components.

Fluorescence anisotropy

Frequency-domain fluorescence anisotropy measurements were performed on a K2 multifrequency phase and modulation fluorometer (ISS Inc., Champaign, IL, USA). The temperature was maintained at 25 °C and controlled with an accuracy of ±0.1 °C using a circulating water bath. Time-resolved fluorescence lifetime and anisotropy measurements were performed in the frequency-domain using the cross-correlation technique (5,6). Excitation of dansyl-labeled CaM was accomplished by use of a 370 nm laser diode (ISS Inc., Champaign, IL, USA; with 370 $\pm$ 10 nm excitation filter) directly connected to a function generator, yielding intensity-modulated excitation light over a frequency range of 2–173 MHz at a cross-correlation frequency of 400 Hz. For modulation, a RF signal of +13 dBm was used. The dansyl emission was collected through a 400 nm long-pass filter. Fluorescence lifetime measurements at magic-angle conditions have been performed prior to the anisotropy experiments in 5 mm path-length quartz cuvettes. The excitation light was vertically polarized (0°), while the emission polarizer was set to an angle of 54.7°. The fluorescence of POPOP was used as lifetime reference (τ = 1.35 ns in ethanol). For the anisotropy experiments, the excitation light was vertically polarized, whereas the polarized emission components were recorded at polarization angles of 0° and 90°. The corresponding phase and modulation data were measured as a function of the modulation frequency.

In frequency-domain lifetime measurements, the shape of the frequency response is determined by the number of decay times displayed by the sample. Since the frequency response is not simple, a single-exponential decay is not sufficient for analysis of the data. Dansyl-labeling of CaM was performed by covalently attaching the dansyl group of dansyl chloride to a lysine residue of CaM. However, it can also react with the phenol group of tyrosine. Thus, the fluorescence lifetime of the dansyl group is different for the sulfonamide or sulfate binding type since it strongly depends on solvent polarity. Based on that, a biexponential decay of dansyl-labeled CaM can be explained by either dansyl groups that were located at two different lysines or bound to lysine and tyrosine. However, for proper analysis – especially when working with large unilamellar lipid vesicles – scattered light has also to be taken into account. Therefore, the phase angle and modulation data obtained in the fluorescence lifetime measurements were fitted using a triexponential decay model that includes two discrete lifetime components for dansyl-CaM and a discrete component fixed at 0.01 ns to account for scattered light:

$$I(t) = \alpha_1 \exp(-t/\tau_1) + \alpha_2 \exp(-t/\tau_2) + \alpha_3 \exp(-t/\tau_3), \quad \text{(S3)}$$

in which τ_1, τ_2, and τ_3 are the fluorescence lifetimes and the pre-exponentials α_1, α_2, and α_3 are the corresponding amplitudes. Thereby, τ_1 was fixed at 0.01 ns to account for scattered light. Nevertheless, the amount accounting for scattered light is rather small in all measurements ($\leq$ 8%). Fits were performed with phase delay errors and modulation ratio errors set to 0.20° and 0.0040, respectively. From the parameters obtained the average fluorescence lifetime, $\langle\tau\rangle$, of the dansyl label can be calculated:

$$\langle \tau \rangle = f_1\tau_1 + f_2\tau_2 + f_3\tau_3 , \quad \text{(S4)}$$

with f_1, f_2, and f_3 indicating the fractional contributions, which can be calculated from fluorescence lifetimes and the corresponding amplitudes by using the following equation:

$$f_i = \alpha_i \tau_i / \sum_i \alpha_i \tau_i \, . \qquad \text{(S5)}$$

The quality of the fit over the entire frequency range was determined by a nonlinear least squares algorithm and reduced χ^2 values were obtained in a range from 1 to 10. Representative fits are given in Fig. S5.

For anisotropy decay determination, differential polarized phase angles and modulation ratios were fitted to a biexponential model:

$$r(t) = r_0\left[g_1 \cdot \exp\left(-t/\theta_1\right) + g_2 \cdot \exp\left(-t/\theta_2\right)\right] = r_{0,1} \cdot \exp(-t/\theta_1) + r_{0,2} \cdot \exp(-t/\theta_2) \;, \qquad \text{(S6)}$$

in which r_0 is the maximum anisotropy. θ_1 and θ_2 account for the reorientational times of the dansyl label (being related to the segmental motion of the label) and the overall rotation of the protein that is equivalent to the overall rotational correlation time, $\theta_{protein}$, of dansyl-labeled Ca^{2+}/CaM. The parameter g_1 and g_2 are the associated fractional amplitudes of each component in the anisotropy decay ($g_1 + g_2 = 1$), with $r_{0,1} = r_0 \cdot g_1$ and $r_{0,2} = r_0 \cdot g_2$. In the fitting process, the previously obtained lifetime data were entered as fixed parameters (cf. Table S1). Fits were performed with delta phase errors and amplitude ratio errors set to 0.20° and 0.0040, respectively. Reduced χ^2 values were obtained in a range of 0.3 to 5.4. Representative fits are given in Fig. S6. Experimental errors were calculated from at least three independent experiments and experimental data were fitted with the VINCI analysis software (ISS Inc., Champaign, IL, USA).

For the protein measurements in solution, dansyl-Ca^{2+}/CaM was diluted with Tris buffer (20 mM Tris, 5 mM $MgCl_2$, 1 mM $CaCl_2$, pH 7.4) to yield a final concentration of 3 μM. First, lifetime and anisotropy data of the protein were measured in the absence of K-Ras4B. Second, K-Ras4B was added in a 1.5 molar ratio ($c_{K\text{-}Ras4B}$ = 2 μM) to the dansyl-labeled Ca^{2+}-loaded CaM and the solution was allowed to incubate for 15 min. Finally, anionic lipid raft vesicles (LUVs composed of DOPC/DOPG/DPPC/DPPG/Chol 20:5:45:5:25 mol%) were added to the K-Ras4B/Ca^{2+}/CaM solution and allowed to incubate for 45 min, yielding a lipid concentration of 0.4 mM (lipid/K-Ras4B ratio of 200:1). Lifetime and anisotropy data were determined for dansyl-Ca^{2+}/CaM after every incubation step. According to the (rotational) Stokes−Einstein relation, the rotational correlation time, $\theta_{protein}$, determined experimentally is proportional to the size (hydrodynamic volume) of the fluorescent protein, i.e., the danysl-labeled Ca^{2+}/CaM. Since the detected value of θ = 9.4 ns for dansyl-labeled Ca^{2+}/CaM in buffer solution (cf. Fig. 4 and Table S2) is significantly larger than that calculated for an equivalent hydrated spherical protein with a molecular volume of 32.4 nm^3 (θ = 7.0 ns) (7), a nonspherical form of monomeric Ca^{2+}-bound CaM has to be assumed, which is in agreement with its known dumbbell shape. The molecular weight is 17 kDa for dansyl-CaM and 21 kDa for K-Ras4B.

RESULTS

Lateral segregation of K-Ras4B and CaM in heterogeneous membranes

To gain complementary spatial information on the single molecule level with an imaging technique, time-lapse tapping mode atomic force microscopy (AFM) experiments were carried out. The protein−membrane interaction process was followed by imaging the same membrane region at various time points. Formation of a coherent, defect-free anionic lipid raft membrane on mica has been assured before addition of protein (cf. Figs. S8 and S9). The solid-supported lipid bilayer segregates into liquid-ordered (l_o) and liquid-disordered (l_d) domains at ambient conditions, which is characterized by a height difference of the two phases of about 1.0 nm (8,9) (Fig. S7).

To assess the membrane extraction process, at first K-Ras4B was added to the membrane, followed by subsequent addition of Ca^{2+}/CaM (Fig. S8). Thereby, protein-enriched domains could be observed within the l_d phase for both GDP- and GTP-bound K-Ras4B (Fig. S8 *B* and *E*, respectively). A mean height of the protein clustered domains of 1.0 ± 0.2 nm and 1.4 ± 0.3 nm with respect to the pure l_d phase was determined for K-Ras4B GDP and K-Ras4B GTP, respectively. These values are in agreement with previous AFM studies of our group that focused on the membrane localization of K-Ras4B (1,2). In analogous measurements of Ca^{2+}/CaM, no significant amount of protein could be detected in the membrane, indicating that Ca^{2+}/CaM does not bind to the anionic lipid raft membrane (Fig. S9 panels *E* and *F*). After injection of Ca^{2+}/CaM solution into the AFM fluid cell containing the K-Ras4B loaded membrane, no substantial changes could be observed for the membrane binding of both K-Ras4B GDP and K-Ras4B GTP (Fig. S8 *C* and *F*, respectively). The mean thickness of the K-Ras4B-enriched domains was also not considerably affected by addition of Ca^{2+}/CaM (K-Ras4B GDP: 1.6 ± 0.3 nm; K-Ras4B GTP: 1.8 ± 0.4 nm). Hence, these results suggest that Ca^{2+}/CaM cannot release K-Ras4B from solid-supported lipid membranes to a significant extent, which might be, for example, due to an effect of the solid support on the immobilized lipid bilayer, since the membrane-support separation is only 0.5–2.0 nm in buffer solution. This could induce steric constraints that might impede the displacement of the proteins. Generally, lower diffusion coefficients are detected in solid-supported membranes as compared to free-standing lipid bilayers of the same composition. Moreover, the large K-Ras4B clusters observed under these conditions in the AFM images may restrict efficient binding of Ca^{2+}/CaM to membrane-anchored K-Ras4B and thus impede K-Ras4B membrane extraction.

However, when the complex of K-Ras4B and Ca^{2+}/CaM, which was preformed in solution, was added to the anionic lipid raft membrane, the AFM images showed a considerably lower amount of K-Ras4B clusters (Fig. S9 *B* and *D*). This indicates that Ca^{2+}/CaM is able to bind K-Ras4B in solution and obstructs binding of K-Ras4B to the membrane, independent of the nucleotide state of K-Ras4B. Corroborated by the IRRAS and fluorescence anisotropy experiments, which also revealed no membrane interaction of the K-Ras4B–Ca^{2+}/CaM complex, we can conclude that binding of the strongly negatively charged Ca^{2+}/CaM to the polybasic stretch of K-Ras4B reverses its charge, preventing binding of the complex to the anionic model raft membrane due to repulsive interactions.

FIGURES

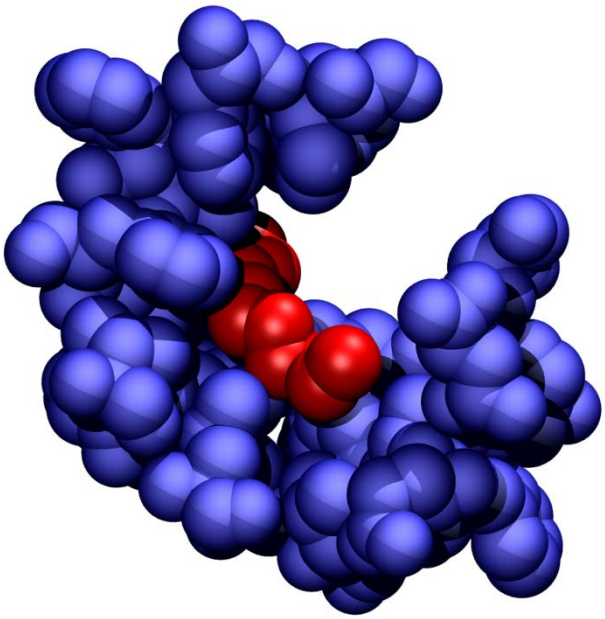

FIGURE S1 Binding interface of the myristoyl group in the hydrophobic tunnel of the CaM complex (PDB code: 1L7Z). Each atom of the corresponding Ca^{2+}/CaM residues is represented by a blue sphere scaled to its van der Waals radius. The volumetric distribution is shown within a distance of 7 Å; the myristoyl group is displayed in red. The image was generated by use of the molecular visualization program VMD (10).

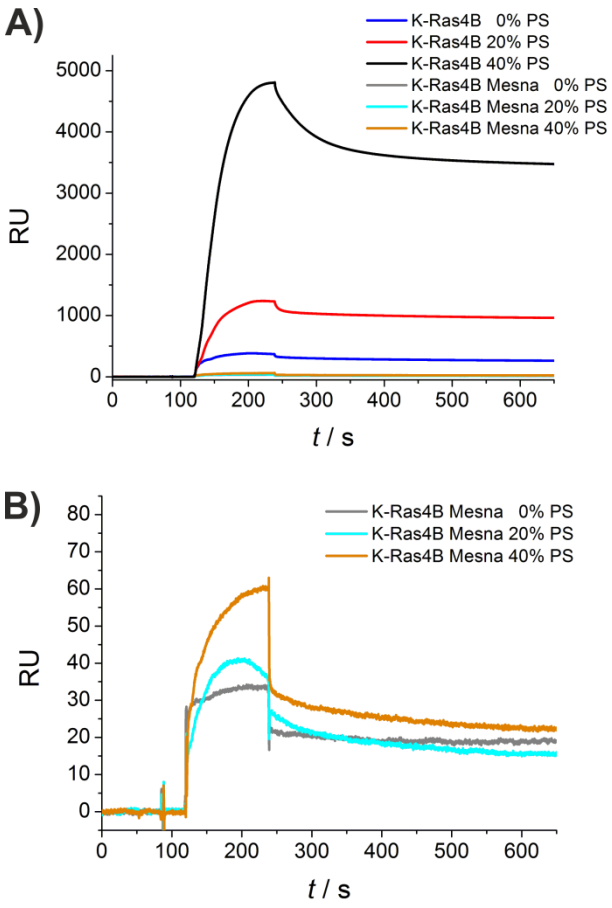

FIGURE S2 SPR sensorgrams of the binding of farnesylated and non-farnesylated, GDP-loaded K-Ras4B to lipid membranes consisting of POPC (0% PS), POPC/POPS 80:20 (20% PS), and POPC/POPS 60:40 (40% PS). (*A*) The sensorgrams clearly demonstrate a charge-dependent membrane binding of farnesylated K-Ras4B, whereas no significant membrane binding was observed for non-farnesylated K-Ras4B (termed K-Ras4B Mesna). (*B*) A detailed view also reveals no significant charge dependency for the membrane interaction of non-farnesylated K-Ras4B, contrary to the membrane interaction behavior of farnesylated K-Ras4B.

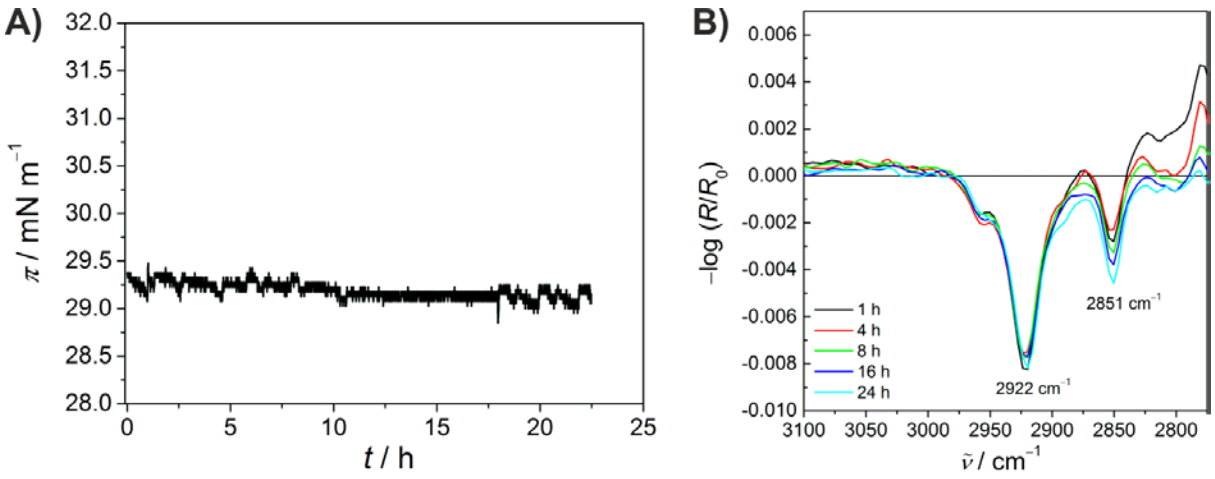

FIGURE S3 Long-term stability of the pure lipid monolayer film at the air-D_2O interface. (*A*) The surface pressure versus time course of the anionic raft-like lipid monolayer (DOPC/DOPG/DPPC/DPPG/Chol 20:5:45:5:25; molar ratio). The lipid film was spread at 29.5 mN m^{-1} at 20 °C. (*B*) IRRA spectra depicting the CH_2 asymmetric (at 2922 cm^{-1}) and symmetric (at 2851 cm^{-1}) vibrations of the lipid acyl chain region of the anionic lipid monolayer over a time period of 24 h. Both parameters remained essentially constant over the entire time period of the IRRAS experiment, implying long-term stability of the anionic lipid monolayer film. All IRRA spectra were acquired at 20 °C with p-polarized light at an angle of incidence of 35°.

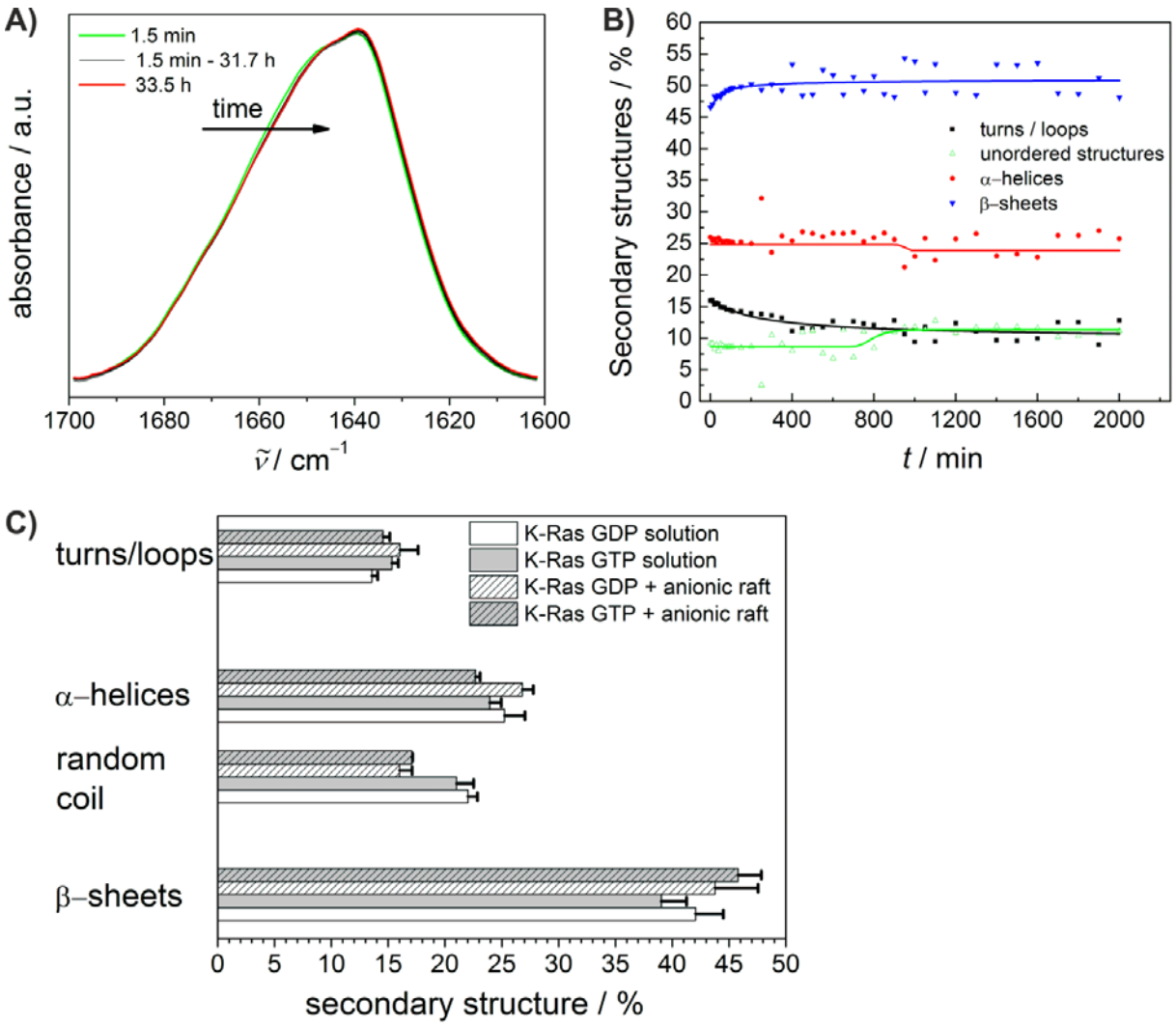

FIGURE S4 Long-term stability of GDP- and GTP-loaded K-Ras4B as analyzed by transmission FT-IR spectroscopy. (*A*) The normalized FTIR spectra for the time evolution of the amide-I′ band of K-Ras4B GTP in the presence of anionic lipid raft membranes composed of DOPC/DOPG/DPPC/DPPG/Chol 20:5:45:5:25 at 25 °C. (*B*) Temporal changes in the structure of K-Ras4B GTP upon interaction with anionic lipid raft bilayers. The secondary structure content was obtained by curve-fitting of the normalized amide-I′ band with a Boltzmann distribution function using the software Origin Pro 7.0. The goodness of fit was in the range of 99.2-99.6%. (*C*) Secondary structure contributions of K-Ras4B bound to different nucleotide states in bulk solution and upon interaction with anionic lipid raft vesicles at 25 °C. The concentration of each protein was 0.233 mM, with a protein to lipid ratio of 1:100. The results are an average of three experiments. The long-term stability of K-Ras4B proteins was ensured in the absence and presence of membranes by detecting no significant changes in secondary structure over the whole time range covered.

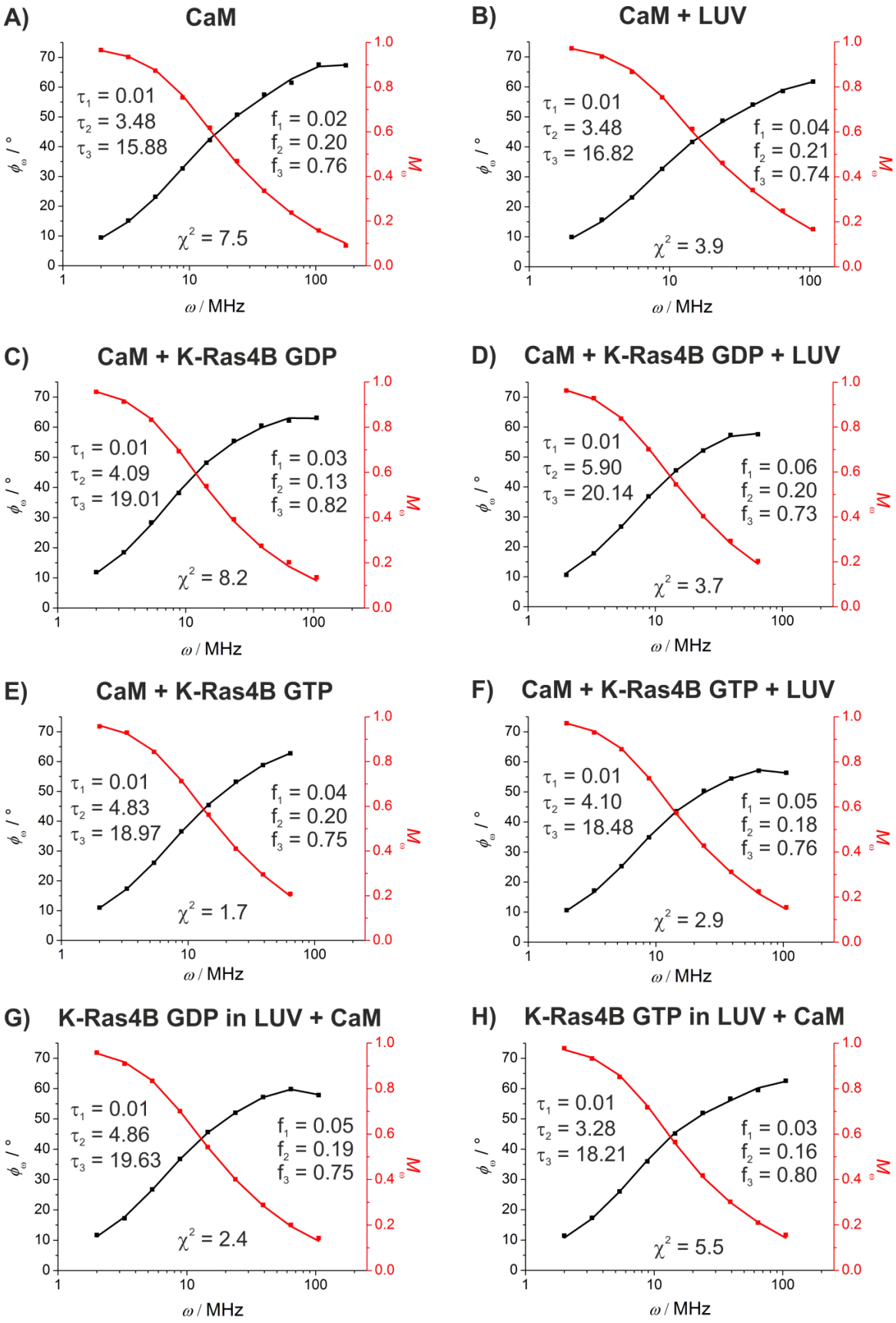

FIGURE S5 Representative phase angle, ϕ_{ϖ}, and modulation, M_{ϖ}, data for dansyl-labeled CaM under the different experimental conditions (black and red squares, respectively). The corresponding fits are shown as solid lines and all values are summarized in Table S1.

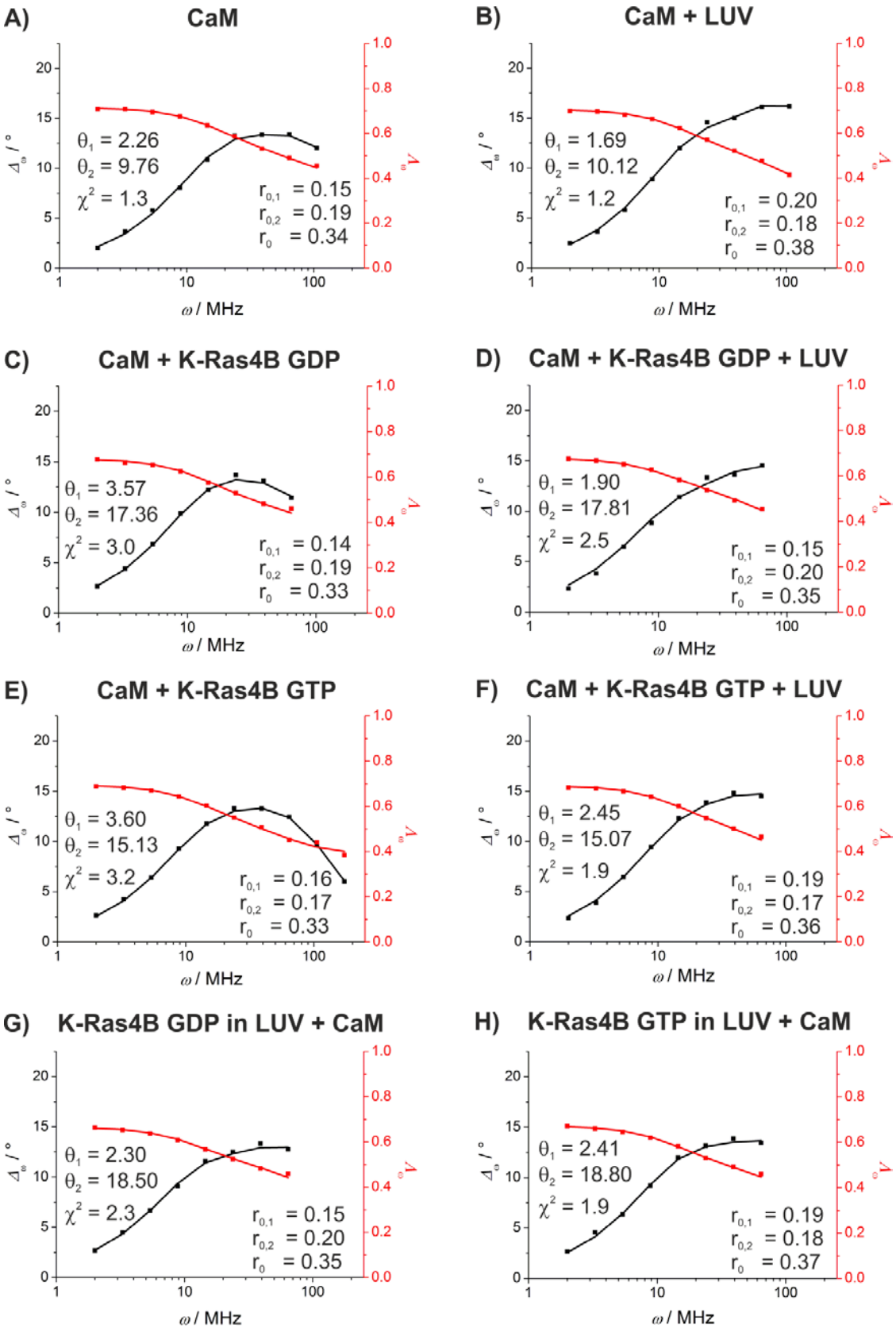

FIGURE S6 Representative differential phase, Δ_ω, and modulation ratio, Λ_ω, data for dansyl-labeled CaM under the different experimental conditions (black and red squares, respectively). The corresponding fits are shown as solid lines and all values are summarized in Table S2.

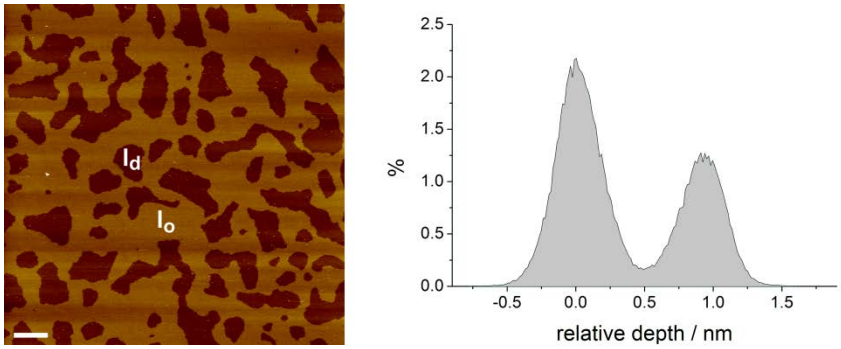

FIGURE S7 AFM image of a lipid membrane on mica consisting of DOPC/DOPG/DPPC/ DPPG/Chol 20:5:45:5:25 (mol%) before injection of protein solution into the AFM fluid cell. The scale bar corresponds to 1 μm. The depth histogram of the AFM image is shown on the right. The difference of the thickness between the l_d and l_o phase, determined from the AFM depth histogram, was 0.9 nm. Previous results confirmed a height difference between both phases of ~1 nm (2).

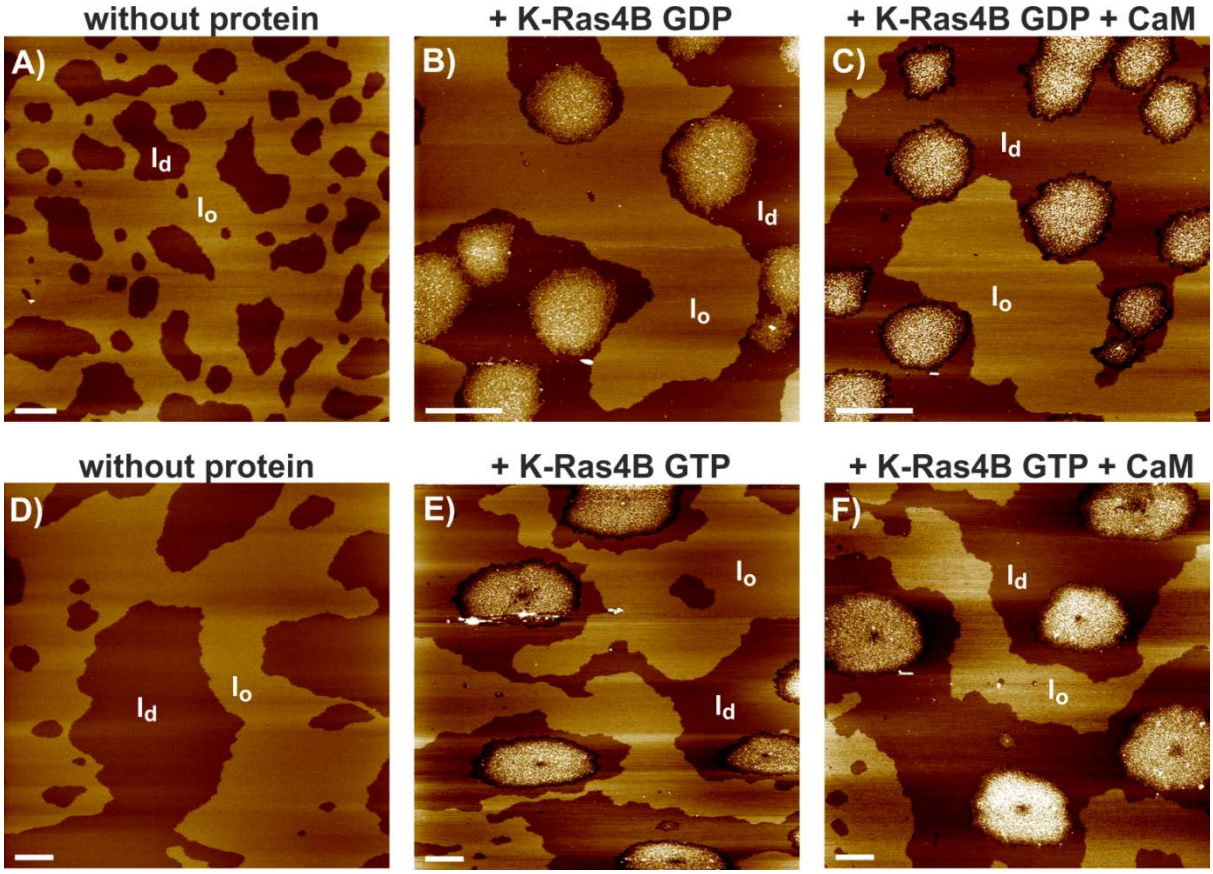

FIGURE S8 AFM images of the interaction of K-Ras4B GDP and K-Ras4B GTP with anionic raft membranes and subsequent addition of Ca^{2+}/CaM. Representative AFM images are shown before (panels *A* and *D*) and after injection of 800 μL K-Ras4B solution ($c_{K\text{-}Ras4B}$ = 0.2 μM) across the lipid membrane in the AFM fluid cell (panels *B* and *E*). After the formation of K-Ras4B-enriched domains in the l_d phase of the phase-separated membrane, a Ca^{2+}/CaM solution was injected into the AFM fluid cell (panels *C* and *F*) to study the effect of Ca^{2+}/CaM on membrane-bound K-Ras4B GDP/GTP. The overall height of the vertical color scale from dark brown to white corresponds to 8 nm for all images and the scale bar represents 1 μm.

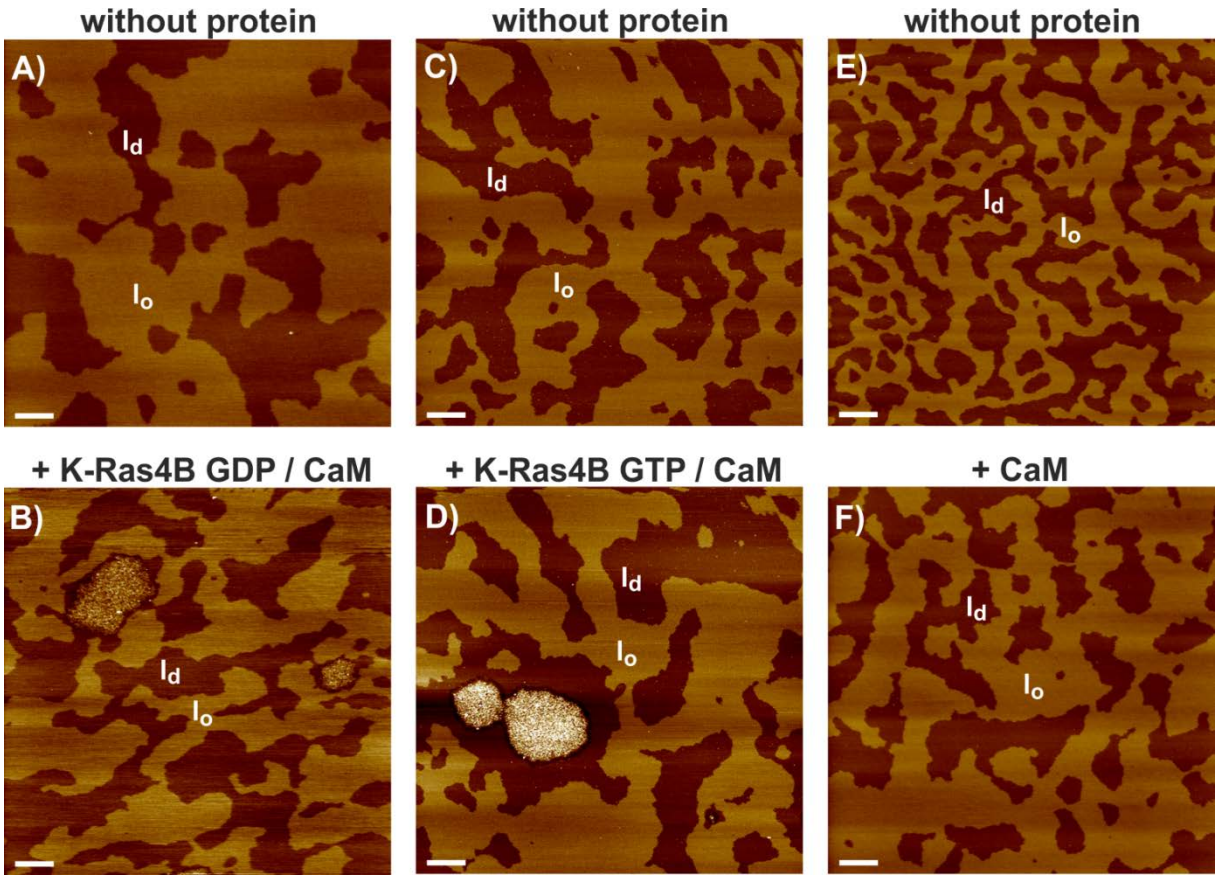

FIGURE S9 Effect of Ca^{2+}/CaM on the interaction of K-Ras4B GDP/GTP with anionic raft membranes. Representative AFM images are shown for the membrane interaction of the premixed K-Ras4B–Ca^{2+}/CaM complex (molar ratio 2:3) after ≈1 h of protein addition to the membrane (panel *B* and *D* for inactive and active K-Ras4B, respectively). Corresponding images before the addition of proteins are shown in panels (*A*) and (*C*). Panels (*E*) and (*F*) display representative AFM images of the anionic lipid raft membrane before and after injection of 800 μL Ca^{2+}/CaM (c = 0.3 μM) into the AFM fluid cell, respectively, indicating no membrane binding of Ca^{2+}/CaM. The overall height of the vertical color scale from dark brown to white corresponds to 8 nm for all images and the scale bar represents 1 μm.

TABLES

Table S1: Results of the fluorescence lifetime analysis. The fluorescence lifetimes τ_1 and τ_2 of dansyl-labeled, Ca^{2+}-loaded CaM and the corresponding fractional contributions f_1 and f_2 are given with the mean value ± standard deviation. Reduced χ^2 values were obtained in a range from 1 to 10.

	f_1	τ_1 / ns	f_2	τ_2 / ns	f_3	τ_3 / ns
CaM	0.03 ± 0.01	0.01	0.21 ± 0.02	3.50 ± 0.38	0.75 ± 0.02	15.93 ± 0.39
CaM + LUV	0.04 ± 0.00	0.01	0.22 ± 0.01	3.74 ± 0.35	0.73 ± 0.02	16.98 ± 0.33
CaM + K-Ras4B GDP	0.03 ± 0.01	0.01	0.17 ± 0.04	4.56 ± 1.16	0.78 ± 0.03	19.23 ± 1.27
CaM + K-Ras4B GTP	0.04 ± 0.01	0.01	0.19 ± 0.03	4.80 ± 0.65	0.76 ± 0.03	19.35 ± 0.56
CaM + K-Ras4B GDP + LUV	0.05 ± 0.01	0.01	0.20 ± 0.02	4.96 ± 0.95	0.74 ± 0.02	19.79 ± 0.71
CaM + K-Ras4B GTP + LUV	0.06 ± 0.02	0.01	0.21 ± 0.02	4.84 ± 1.22	0.73 ± 0.03	19.33 ± 0.85
K-Ras4B GDP in LUV + CaM	0.04 ± 0.02	0.01	0.19 ± 0.03	4.06 ± 1.33	0.77 ± 0.04	19.30 ± 0.65
K-Ras4B GTP in LUV + CaM	0.03 ± 0.01	0.01	0.17 ± 0.02	3.35 ± 0.38	0.79 ± 0.02	18.44 ± 0.52

Table S2: Results of the fluorescence anisotropy analysis. Rotational correlation times θ_1 and θ_2 (with θ_2 being equal to the overall rotational correlation time of the protein, i.e., $\theta_2 = \theta_{\text{dansyl-CaM}}$) of danysl-labeled, Ca^{2+}-loaded CaM and corresponding values for $r_{0,1}$ and $r_{0,2}$ are shown with the mean value ± standard deviation. Reduced χ^2 values were obtained in a range from 0.3 to 5.4.

	$r_{0,1}$	θ_1 / ns	$r_{0,2}$	θ_2 / ns	r_0
CaM	0.15 ± 0.03	1.97 ± 0.54	0.20 ± 0.02	9.44 ± 0.87	0.35 ± 0.02
CaM + LUV	0.19 ± 0.06	1.87 ± 0.73	0.18 ± 0.06	10.13 ± 2.73	0.37 ± 0.01
CaM + K-Ras4B GDP	0.15 ± 0.02	3.62 ± 0.60	0.19 ± 0.02	17.87 ± 1.29	0.33 ± 0.01
CaM + K-Ras4B GTP	0.15 ± 0.02	3.68 ± 0.69	0.18 ± 0.02	16.06 ± 2.09	0.33 ± 0.01
CaM + K-Ras4B GDP + LUV	0.19 ± 0.03	2.22 ± 0.60	0.17 ± 0.02	18.01 ± 2.30	0.36 ± 0.01
CaM + K-Ras4B GTP + LUV	0.18 ± 0.03	2.26 ± 0.72	0.18 ± 0.03	16.26 ± 1.70	0.36 ± 0.01
K-Ras4B GDP in LUV + CaM	0.16 ± 0.01	2.47 ± 0.77	0.20 ± 0.02	18.38 ± 0.55	0.36 ± 0.02
K-Ras4B GTP in LUV + CaM	0.19 ± 0.01	2.41 ± 0.58	0.18 ± 0.02	18.30 ± 1.72	0.36 ± 0.02

SUPPORTING REFERENCES

1. Weise, K., S. Kapoor, A. Werkmüller, S. Möbitz, G. Zimmermann, G. Triola, H. Waldmann, and R. Winter. 2012. Dissociation of the K-Ras4B/PDEδ Complex upon Contact with Lipid Membranes: Membrane Delivery Instead of Extraction. *J. Am. Chem. Soc.* 134:11503–11510.
2. Weise, K., S. Kapoor, C. Denter, J. Nikolaus, N. Opitz, S. Koch, G. Triola, A. Herrmann, H. Waldmann, and R. Winter. 2011. Membrane-Mediated Induction and Sorting of K-Ras Microdomain Signaling Platforms. *J. Am. Chem. Soc.* 133:880–887.
3. Gohlke, A., G. Triola, H. Waldmann, and R. Winter. 2010. Influence of the Lipid Anchor Motif of N-Ras on the Interaction with Lipid Membranes: A Surface Plasmon Resonance Study. *Biophys. J.* 98:2226–2235.
4. Kapoor, S., G. Triola, I. R. Vetter, M. Erlkamp, H. Waldmann, and R. Winter. 2012. Revealing conformational substates of lipidated N-Ras protein by pressure modulation. *Proc. Natl. Acad. Sci. USA.* 109:460–465.
5. Gratton, E., and M. Limkeman. 1983. A continuously variable frequency cross-correlation phase fluorometer with picosecond resolution. *Biophys. J.* 44:315–324.
6. Gratton, E., D. M. Jameson, and R. D. Hall. 1984. Multifrequency phase and modulation fluorometry. *Annu. Rev. Biophys. Bioeng.* 13:105–124.
7. Yao, Y., C. Schoneich, and T. C. Squier. 1994. Resolution of structural changes associated with calcium activation of calmodulin using frequency domain fluorescence spectroscopy. *Biochemistry.* 33:7797–7810.
8. Kapoor, S., A. Werkmüller, C. Denter, Y. Zhai, J. Markgraf, K. Weise, N. Opitz, and R. Winter. 2011. Temperature-pressure phase diagram of a heterogeneous anionic model biomembrane system: results from a combined calorimetry, spectroscopy and microscopy study. *Biochim. Biophys. Acta.* 1808:1187–1195.
9. Evers, F., C. Jeworrek, K. Weise, M. Tolan, and R. Winter. 2012. Detection of lipid raft domains in neutral and anionic Langmuir monolayers and bilayers of complex lipid composition. *Soft Matter.* 8:2170–2175.
10. Humphrey, W., Dalke, A. and Schulten, K. 1996. VMD - Visual Molecular Dynamics. *J. Molec. Graphics.* 14:33–38.